Available online at www.sciencedirect.com
ScienceDirect
European Journal of Mechanics B/Fluids 27 (2008) 177–201

Spin-up and spin-down dynamics of a liquid metal driven by a single rotating magnetic field pulse

Petr A. Nikrityuk [a,*], Sven Eckert [b], Kerstin Eckert [a]

[a] *Institute for Aerospace Engineering, Dresden University of Technology, D-01062 Dresden, Germany*
[b] *Forschungszentrum Dresden-Rossendorf (FZD), MHD Department, 01314 Dresden, Germany*

Received 10 August 2006; received in revised form 10 May 2007; accepted 22 May 2007

Available online 6 June 2007

Abstract

This paper presents a study concerning the transient dynamics of the flow field inside a liquid metal filling a finite cylindrical container: The flow is created by applying a rotating magnetic field (RMF) in the form of a single pulse. The flow structure is governed by an impulsive spin-up from the rest state which is followed by a spin-down phase, with the fluid in a state of inertia. The pulse length has been found to have a distinct influence on the transient fluid flow. Two cases are considered: an enclosed cavity and a cavity with a free surface, in order to show that in both cases the recirculating flow in the radial-meridional plane displays periodical reversals. This phenomena is especially pronounced if the pulse length of the electromagnetic forcing corresponds to the so-called initial adjustment phase as defined by Nikrityuk, Ungarish, Eckert, Grundmann [P.A. Nikrityuk, M. Ungarish, K. Eckert, R. Grundmann, Spin-up of a liquid metal flow driven by a rotating magnetic field in a finite cylinder. A numerical and analytical study, Phys. Fluids 17 (2005) 067101–0671016].

PACS: 47.65

Keywords: Spin-up; Spin-down; Rotating fluids; Liquid metal; Rotating magnetic field

1. Introduction

Rotating magnetic fields (RMFs) are widely used in the metallurgical and semiconductor industries to eliminate flow asymmetries and to control heat and mass transfer toward the solidification front [2,1]. This effect is based on the swirling flow, which is often called the primary flow, induced directly by RMF. In the case of a finite liquid metal column this primary flow produces the secondary (meridional) flow in the form of two toroidal vortices due to the Ekman pumping effect [2,3]. The application of an RMF-driven convection during the solidification of metal alloys has therefore been proved as a striking method for mixing alloy components or provoking a distinct grain refining effect [4]. However, on the other hand, a rotary stirring of this kind also causes distinct macrosegregations [5], resulting from a strong radial flow in the mushy zone. Obviously, the control of the flow field during solidification is of major

* Corresponding author.
E-mail addresses: nikrityuk@tfd.mw.tu-dresden.de (P.A. Nikrityuk), S.Eckert@fz-rossendorf.de (S. Eckert).

0997-7546/$ – see front matter
doi:10.1016/j.euromechflu.2007.05.004

industrial importance to obtain castings without segregation. In analogy to the mechanical intermittent rotation of a container with the melt proposed by Neilson and Incropera [6], an alternative to solve the problem is periodically spin up and spin down the liquid motion by an RMF which is discontinuous in time. That means, for example, that the RMF is switched on and off periodically. The main idea is to provoke periodic reversals of the flow ahead of the solidification front in order to avoid a continuous, convective transport of solute, which is rejected by the solidifying alloy, exclusively in one direction. It is a well-known fact that such periodic reversals of the secondary flow occur over a period of time while the rotating flow undergoes a spin-up or spin-down motion [3,7]. This idea is employed to counteract the critical influence of buoyancy-driven convection on segregation and morphological stability by means of a mechanical rotation of the melt crucible in crystal growth technologies such as so-called accelerated crucible rotation (ACRT) [8,9] and the angular vibration techniques (AVT) [10]. All these techniques are based on a periodic alteration of the rotation rate of the rigid vessel walls. In this case the interior flow experiences a so-called classic spin-up and spin-down.

Here one has to distinguish between the classic and the RMF-driven spin-up and spin-down. By classic spin-up we refer to all those cases in which the forcing is provided by moving solid boundaries. Pertinent studies are reviewed by Duck and Foster [11]. In contrast to the classic spin-up, the RMF provides a volume force (Lorentz force). In other words, the value of angular velocity of the liquid Ω has to be considered as a solution to the problem of RMF stirring and not as a boundary condition. The classic spin-down process, where the fluid container is brought to rest impulsively, has already been studied in detail by Neitzel and Davis [7], Valentine and Miller [12], Lopez and Weidman [13] and Cui [14] amongst others. The main difference between the classic spin-down and the spin-down arising from a shut-down of the RMF comes from the initial conditions. Whereas the analysis of a classic spin-down starts from the solid-body rotation, a rotary electromagnetic stirring in a finite vessel always includes a recirculation. Additionally, the flow developed at sufficiently high magnetic field intensities (as considered in this study) also comprises Taylor–Görtler vortices.

Only a few studies are available which are devoted to intermittent, rotary electromagnetic stirring. Kojima et al. [15] published an experimental study considering the impact of intermittent and alternate stirring on the center segregation of casting blooms. Under certain conditions they found a reduction of the segregation and they were able to verify the incidence of flow reversals for their stirring conditions. Analytical and numerical studies were carried out by Davidson [16] and Davidson and Boysan [17]. They showed that a strong oscillatory recirculation develops in the period between successive applications of the RMF. The initial axial gradient in the swirl was identified as driving this recirculation. These findings give a first insight into the fluid mechanics in intermittent stirring. But since artificial non-uniform swirl distributions and zero recirculation were used as the initial conditions at the beginning of spin-down, the results cannot be straightforwardly adopted to realistic RMF-driven flows. Motivated by the lack of knowledge in this field, the subject of the present study is to investigate the transient flow pattern inside a cylindrical liquid metal column affected by an RMF pulse. During this pulse the fluid undergoes an impulsive spin-up, then the RMF is switched off and the flow continues rotating under its own inertia, and decays because of viscous effects. It is obvious that the pulse length appears as a further important parameter here, because the duration of the pulse determines the initial flow field for the spin-down. The problem is treated numerically for both an enclosed cylinder and a cylinder with a free surface. The numerical calculations were accompanied by velocity measurements in a ternary GaInSn alloy by means of the ultrasound Doppler velocimetry.

The paper is organized as follows. In Section 2, the problem formulation and the mathematical model are presented. Section 3 is devoted to a description of the numerical techniques. Section 4 describes the experimental set-up. Section 5 contains the results obtained from numerics and experiment. The first subsection is devoted to the analysis of transient dynamics of the fluid flow induced by an RMF pulse in an enclosed cylinder. The second subsection gives insights into the flow characteristics depending on the RMF pulse duration for the case of the cavity with free surface. The influence of the aspect ratio of the cavity is discussed in Appendix A.

2. Problem formulation

The numerical handling of the problem under consideration requires several main simplifications. *First*, the RMF is spatially homogeneous and the symmetry axis of the RMF and the cylindrical cavity are identical. *Second*, the RMF fulfills the low-frequency and the low-induction approximation, see Section 2.1. *Third*, the flow is axisymmetric. For the low-frequency, low-induction RMF this assumption is satisfied for $Ta < Ta_{\mathrm{cr}}^{\mathrm{3D}}$ due to the laminar flow regime.

Here Ta and Ta_{cr}^{3D} are the magnetic Taylor number, see Eq. (1), and the critical magnetic Taylor number at which the RMF-driven flow becomes unstable with respect to three-dimensional perturbations [18]. For $Ta > Ta_{cr}^{3D}$ as considered in this work, the flow is assumed to be axisymmetric during the first few revolutions of the fluid. Thus, as a first approach we use the axisymmetric numerical simulation (ANS) model introduced by Randriamampianina et al [19]. We note that the validity of the axisymmetry assumption applied to the RMF-driven turbulent flows was demonstrated recently by Nikrityuk et al. [20,21], who showed that the use of ANS for the modelling of time-averaged quantities of the turbulent flow regime for $Ta > Ta_{cr}^{3D}$ provides a very good agreement with experimental [39] and 3D DNS data [40].

We emphasize that if the first assumption is not fulfilled, the relevance of the third assumption is questionable. To be precise, an asymmetric positioning of the magnetic system with respect to the symmetry axis of the cavity may provoke an azimuthal dependence of the flow field even during the first revolutions of the liquid metal column. This scenario is undesired for the industrial applications because it may automatically lead to inhomogeneous distributions of the temperature and the mass concentration of material components in an azimuthal direction. The question regarding the influence of small deviations between the symmetry axis of RMF and the cavity on the asymmetry of the flow is still open in the literature and requires 3D DNS which is beyond the scope of this work.

2.1. Rotating magnetic field and scale parameters

We consider the application of a uniform rotating magnetic field (RMF), characterized by a component of the magnetic field induction with the amplitude B_0 directed in a radial direction, only. It rotates with the angular frequency $\omega_0 = 2\pi f$ (f is the frequency of the alternating current) in an isothermal liquid metal filled into a vertically oriented cylindrical vessel with an inner radius R_0 and a height H_0 corresponding to the aspect ratio of unity. The cylinder walls are made from an electrically insulating material. In this work we consider both an enclosed cylinder and a cylinder with a free surface. A principle scheme showing the interaction between the RMF and a liquid metal column is displayed in Fig. 1(a). On referring to the work of Marty et al. [22], the maximal time-averaged electric current density induced by the RMF flows along a meridional perimeter of a cylinder and rotates with an angular velocity ω_0. The product of $j_z \cdot B_r$ provides the azimuthal component of the Lorentz force, F_L, which makes the fluid rotate.

The effect of an RMF on the electroconductive liquid can be described by the following dimensionless quantities [2,23]:

(a) the Reynolds number corresponding to the magnetic field rotation $Re_\omega = \omega_0 R_0^2/\nu$,
(b) the Hartmann number based on the effective magnetic field induction $Ha = (B_0/\sqrt{2})R_0\sqrt{\sigma/(\rho\nu)}$,
(c) the shielding parameter $\bar{\omega} = \mu_0\sigma\omega_0 R_0^2$, and
(d) the aspect ratio of the cylinder $A = 2R_0/H_0$.

Here, ρ, ν and σ, respectively, refer to the density, the kinematic viscosity and the electrical conductivity of the liquid and μ_0 stands for the magnetic permeability. Ha and Re_ω can be unified to the magnetic Taylor number given by:

$$Ta = Ha^2 Re_\omega = \frac{\sigma B_0^2 \omega_0 R_0^4}{2\mu\nu}. \tag{1}$$

As already mentioned before the RMF frequency, ω_0, and the magnetic field induction, B_0, are constrained to the so-called low-frequency low-induction conditions. Namely, the RMF frequency is low enough so that the skin depth is larger than R_0 ($\bar{\omega} < 1$) and the angular velocity of a liquid, Ω, induced by the RMF does not change the magnetic field applied. It is satisfied since $Ha^4/Re_\omega \gg 1$, see Ref. [24]. Note that the low-induction condition corresponds automatically to the case when the magnetic Reynolds number is less than unity ($Re_m = \sigma\mu_0\Omega R_0^2 \ll 1$). The criterion for estimating of the influence of the fluid flow on the electric potential induced by an RMF, and with it the Lorentz force, is the so-called interaction parameter, $N = \sigma B_0^2/\rho\Omega$, see Ref. [2]. If $N \ll 1$ the Lorentz force can be decoupled from the fluid flow. Under these conditions the action of the RMF in electroconductive homogeneous media can be described by a purely azimuthal time-averaged body force, which has an analytical expression. The meridional component of the Lorentz force has a minor effect on the fluid flow in comparison to the azimuthal component [24],

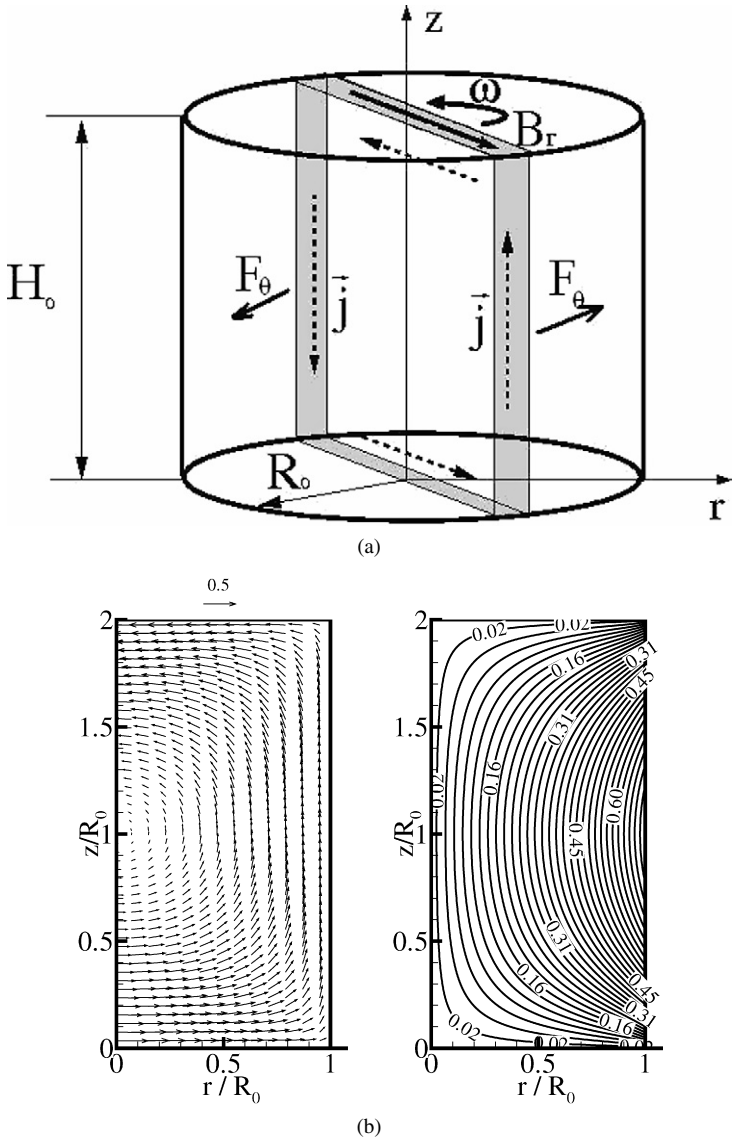

Fig. 1. (a) Scheme of the interaction of an RMF and a liquid metal; (b) Contour plot of the Lorentz force scaled with $0.5B_0^2\omega_0 R_0\sigma$ (left) and vector plot of the time-averaged electric current density scaled with $\omega_0 B_0 R_0\sigma$.

thus we neglect it. The azimuthal component of the Lorentz force is a function of the position only and takes the following form [25]:

$$F_L = \frac{1}{2}\sigma\omega_0 B_0^2 r\left(1 - \frac{2}{r'}\sum_{k=1}^{\infty}\frac{J_1(\zeta_k r')\cosh(\zeta_k(z' - \frac{1}{2}H'))}{(\zeta_k^2 - 1)J_1(\zeta_k)\cosh(\frac{1}{2}\zeta_k H')}\right) \tag{2}$$

where $z' = z/R_0$, $r' = r/R_0$, $H' = H_0/R_0$, J_1 is the Bessel function of the first kind and ζ_k are the roots of $J_1'(x) = 0$. To be precise, the Lorentz force is composed of two parts: a mean axisymmetric component given by Eq. (2) and a time-dependent one, oscillating at twice the original frequency. The latter only marginally affects the fluid flow [26] at frequencies considered here and is therefore neglected in this work, too. The spatial distributions of the electric current density and the azimuthal Lorentz force induced by the low-frequency low-induction RMF are shown in Fig. 1(b). It can be seen that the product of the non-axisymmetric current density, j_z, and the radial component of the magnetic

Table 1
The values of the characteristic times and velocities in nondimensional form for $A = 1$ and various Taylor numbers. The meaning of the particular times is explained in the text

B (mT)	Ta	E_{ce}	E_{ia}	Ω_{ce} (s^{-1})	t_{ia}/t_{ref}	t_{ref} (s)	$t_{spin\text{-}up}$ (s)	$CV_r \times CV_z$	Δt
0.6	1.06×10^5	1.0×10^{-3}	3.40×10^{-3}	0.53	4.61	3.99	118.02	100×200	0.1
0.9	2.39×10^5	6.0×10^{-4}	2.27×10^{-3}	0.91	4.44	2.66	90.07	120×240	0.1
2	1.18×10^6	2.1×10^{-4}	1.07×10^{-3}	2.63	4.33	1.2	52.89	120×240	0.1
3	2.65×10^6	1.2×10^{-4}	7.16×10^{-4}	4.51	4.31	0.8	40.36	120×240	0.05

field induction provides the axisymmetric azimuthal component of the Lorentz force. For the calculation of 2D plots of these quantities we used data from the work of Nikrityuk, Eckert and Grundmann [27].

We note that in the case of a cavity with a flat free surface, Eq. (2) can be used to model the fluid flow induced by the RMF (if the low-induction condition and $N \ll 1$ are fulfilled). The validation tests showed good agreement with experimental data, see Ref. [28]. To check whether the interaction parameter and magnetic Reynolds number are less than unity we use the core effective angular velocity Ω_{ce} as a characteristic angular velocity [29,30]:

$$\Omega_{ce} = \eta^{4/3}\left[\left(\frac{1}{4c}\right)^{2/3}\Omega_f\left(\frac{\Omega_f H_0^2}{\nu}\right)^{1/3}\right] \tag{3}$$

where $\Omega_f = B_0\sqrt{\sigma\omega_0/\rho}$ is the so-called forcing angular velocity (the term "forcing" comes from Eq. (2), namely $\rho F_L = \frac{1}{2}\Omega_f^2 r(\cdot)$) and c stands for the Bödewadt layer coefficient which is $c = 1.35$. The parameter η describes the axial efficiency of $F_{L\theta}$ and depends strongly on the aspect ratio A, e.g. $\eta = 0.62$ for $A = 1$ but $\eta = 0.312$ for $A = 2$ (cf. [30]). Based on Ω_{ce} the Ekman number can be written as $E_{ce} = \nu/\Omega_{ce}R_0^2$. Recently it was shown that Eq. (3) is a very good prediction of the angular velocities not only for laminar flows [31] but also for turbulent flows driven by an RMF [20]. In this way we can use Ω_{ce} for the following estimation of Re_m and N. Table 1 relates the magnetic induction B_0 used in this work to the corresponding values of Ta and Ω_{ce}, E_{ce}, based on the geometry of the cylindrical cavity and the material properties of Ga–In–Sn: $\rho = 6300$ kg/m^3, $\nu = 3.4 \times 10^{-7}$ m^2/s and $\sigma = 3.5 \times 10^6$ A/V m and a magnetic field frequency of $f = 50$ Hz. We obtain $Re_m \approx 10^{-2}$ and $N \approx 10^{-3}$ for the maximum Ta used in this work. Thus, our assumption about the non-dependence of F_L on the velocity of the liquid is correct.

As a next step we introduce the characteristic time scales which are relevant to spin-up and spin-down problems of RMF-driven flows. The first time scale is the so-called spin-up time, $t_{spin\text{-}up}$ [29,30], which has been identified as the representative time scale required for the flow to spin up into the steady state for $Ta < Ta_{cr}^{3D}$ or to reach a developed turbulent regime for $Ta > Ta_{cr}^{3D}$. The mathematical expression for this time takes the following form:

$$t_{spin\text{-}up} = \frac{H_0}{\sqrt{\nu\Omega_{ce}}}. \tag{4}$$

The second time scale, t_{ref}, describing the meridional flow dynamics, is derived from balancing the inertial and the Lorentz force (e.g. following Marty et al. [22] we can write $\sigma\omega_0 B_0^2 R_0 \approx \rho U_{ref}^2/R_0$, which can be transformed into $U_{ref}/R_0 \approx B_0\sqrt{\sigma\omega_0/\rho} = \Omega_f$), and is given by:

$$t_{ref} = \Omega_f^{-1} = \left(B_0\sqrt{\frac{\sigma\omega_0}{\rho}}\right)^{-1}. \tag{5}$$

Recently it was shown that on the basis of the time history of the volume-averaged meridional velocity given by:

$$U_{rz} = \frac{2}{R_0^2 H_0}\int_0^{H_0}\int_0^{R_0} r\sqrt{u_r^2 + u_z^2}\,dr\,dz \tag{6}$$

that the RMF-driven spin-up can be divided into two phases [30]. The first phase which is always passed through during the spin-up from rest is called the *initial adjustment* (*i.a.*) phase, in which a secondary meridional flow in the form of two toroidal vortices is established. The *i.a.* phase comprises the time interval $0 < t \leqslant t_{ia}$, where t_{ia} marks the moment when the first maximum of U_{rz} appears (see also Section 5). The *i.a.* phase is thus completed on achieving the first maximum in the volume-averaged kinetic energy of the secondary flow corresponding to the time

when $\partial U_{rz}/\partial t = 0$. As was recently shown by Nikrityuk et al. [28,30], the development of the initial adjustment phase usually occurs in a time period of about 3.5–5t_{ref} depending on *Ta*. The duration of the *i.a.* phase and the entire spin-up are summarized in Table 1 for several *Ta*. The Ekman number, E_{ia}, provided in Table 1 was calculated by means of Ω_{ia}, which corresponds to the angular velocity of the liquid, Ω, on the axis of rotation for $z = H_0/2$ at $t = t_{\text{ia}}$.

It should be noted that viscous effects play a negligible role in this initial period ($0 < t < t_{\text{ia}}$) which is followed by the second phase called an *inertial* phase. The duration of this phase takes the interval $t_{\text{ia}} < t \leqslant t_{\text{spin-up}}$. During this phase the development of the meridional flow proceeds via inertial oscillations; for the details we refer to Ref. [30].

2.2. Governing equations

The liquid metal can be considered as a Newtonian incompressible fluid. Buoyancy and Joule dissipation are negligible; the latter becomes important for $Ta > 10^9$ only (Ref. [21]). The continuity and Navier–Stokes equations written in cylindrical polar coordinates (r, θ, z) have been solved:

$$\nabla \cdot \vec{u} = 0, \tag{7}$$

$$\partial_t \vec{u} + (\vec{u}\nabla)\vec{u} = -\frac{1}{\rho}\nabla p + \nu \Delta \vec{u} + \frac{F_L \vec{e_\theta}}{\rho}. \tag{8}$$

The axisymmetry of the problem is impressed by canceling the derivatives with respect to θ. The projection of the momentum conservation equation in the azimuthal direction takes the form:

$$\frac{\partial u_\theta}{\partial t} + u_z \frac{\partial u_\theta}{\partial z} + u_r \frac{\partial u_\theta}{\partial r} = \nu \frac{\partial^2 u_\theta}{\partial z^2} + \frac{\nu}{r}\frac{\partial}{\partial r}\left(r \frac{\partial u_\theta}{\partial r}\right) - \frac{u_r u_\theta}{r} - \nu \frac{u_\theta}{r^2} + \frac{F_L}{\rho}. \tag{9}$$

No-slip conditions are applied on all solid walls. The upper free surface is free of tangential stresses and non-deformable. This boundary condition showed a reasonable agreement between experimental and numerical data [28]. Here, it should be noted that the use of the Navier–Stokes equations written in physical units facilitates the interpretation of the transient dynamics of primary and secondary flows during spin-up and spin-down.

3. Numerical techniques

Eqs. (7) and (8) are computed numerically by an open source code based on the finite-volume method using orthogonal grids [32]. Variable storage is collocated and cell-centered. The SIMPLE pressure-correction algorithm is used to calculate the pressure. The Rhie–Chow stabilization scheme is applied [33]. The convection terms are discretized by a deferred-correction scheme [32]. The diffusion terms were approximated using the second-order central differencing scheme. The systems of linear equations are solved using Stone's strongly implicit procedure [34]. The time derivatives are discretized using a three-time-level scheme. Time marching is realized with a fixed time step. The outer iterations are stopped when the maximal residual is less than 10^{-10} in physical units. Several grid-convergence tests are performed. Details of the time steps and grid resolutions used in this work are also provided in Table 1. The code was validated in Ref. [30].

4. Experimental set-up

Accompanying the numerical simulations, experiments were performed focusing on velocity measurements in RMF-driven liquid metal flows. For this reason the ternary eutectic alloy Ga68In20Sn12 was used, which is liquid at room temperature. A schematic view of the experimental set-up is depicted in Fig. 2. The alloy was poured to a height of $H_0 = 60$ mm into a cylindrical container made from Perspex, likewise with a diameter of $D_0 = 2R_0 = 60$ mm, ensuring an aspect ratio of unity. The cylinder was located concentrically inside a magnetic induction system with a bore diameter of 90 mm and a height of 220 mm. Special care was taken to ensure that the fluid container was positioned precisely, because small deviations from the symmetry (vertical alignment, conformity of both the cylinder and magnetic field axis) would have measurable effects on the flow structure. The magnetic system was able to provide an RMF to a maximum field strength of 25 mT and a frequency in a domain between 10 and 400 Hz. All measurements were carried out at a frequency of 50 Hz, small enough to exclude any influence from the skin effect. Using these magnetic field parameters a maximum magnetic Taylor number of 3.5×10^8 (according to Eq. (1)) can

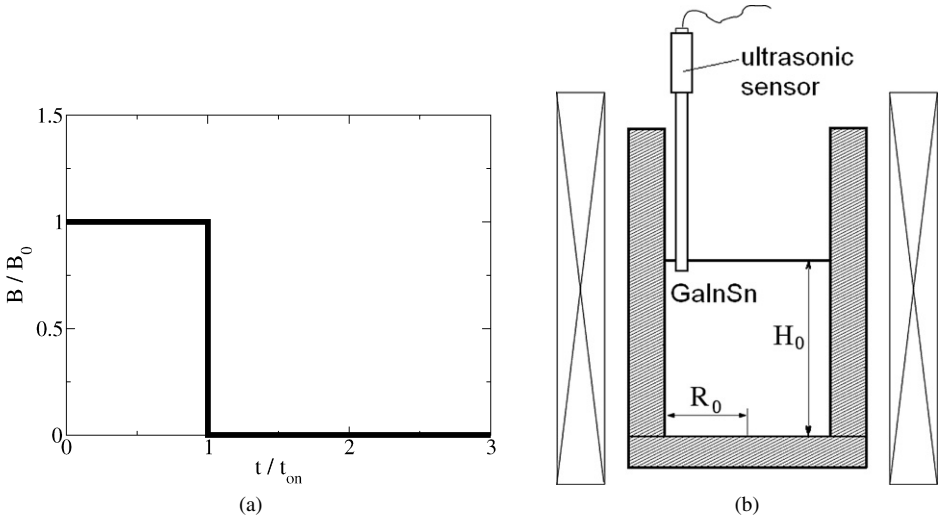

Fig. 2. A scheme of the RMF pulse (a) and the experimental set-up (b).

be achieved. The homogeneity of the magnetic field was checked using a 3-axis Gauss meter (Lakeshore model 560, sensor type MMZ2560-UH). Within a radius of 30 mm, which was selected as the radial dimension of the container, the variance of the magnetic field strength was found to be smaller than 5% with respect to the absolute value of B_0. The vertical velocity component was measured by means of ultrasound Doppler velocimetry (UDV), which is based on the pulsed echo technique and delivers instantaneous profiles of the local velocity along the ultrasonic beam. For a detailed description of the measuring principle we refer to Takeda [35]. In various studies the UDV technique has been shown to be suitable for determinating velocity in liquid metal flows (see for instance [36,37]). An elaborate discussion of specific problems arising in the context of UDV measurements in liquid metals can be found in [38]. In the present experiments the DOP2000 velocimeter (model 2125, Signal Processing SA, Lausanne) and an 8 MHz transducer (TR0805LS, diameter 5 mm) were utilized. The transducer was aligned vertically and attached to the free surface of the liquid metal at a radial position of $r/R_0 = 0.6$. The sensor was located 2.0 ± 0.5 mm beneath the free surface. This set-up allows the measurement of the axial component of the velocity. The measuring volume can be considered as a series of consecutive discs lined up concentrically along the ultrasonic beam. Because of the divergence of the ultrasonic beam the lateral size of the measuring volume increases with the distance from the transducer. Hence, the spatial resolution in a lateral direction varies from 5 mm at the sensor to approximately 7.5 mm at the bottom of the fluid vessel. The spatial resolution in an axial direction was about 1.4 mm. The velocity data were acquired with a sampling frequency of 8.33 Hz. The velocity resolution was about 0.5 mm/s.

5. Results

In this work we study the impact of an RMF pulse of a length t_{on} on the fluid flow dynamics. The scheme of the RMF pulse is shown in Fig. 2(a). The presentation of the results is subdivided into two parts addressing the configuration of an enclosed cylinder and a cylinder with a free surface. Both situations have been examined numerically, whereas experimental findings will be provided for the case of a free surface flow. In the analysis of numerical results we use dimensionless variables which are scaled with the cylinder radius, the azimuthal velocity and the meridional velocity as follows:

$$R_0, \quad \Omega_{\text{ce}} R_0, \quad E_{\text{ce}}^{1/2} \Omega_{\text{ce}} R_0. \tag{10}$$

Correspondingly, $t_{\text{spin-up}}$ (see Eq. (4)) and t_{ref} (Eq. (5)) have been used as typical time scales for the primary and meridional flow, respectively. Furthermore, in the text and figures the prime ($'$) denotes the dimensionless variables with respect to the scaling (10).

5.1. Enclosed cylinder: spin-up and spin-down at constant RMF pulse length

The first part of our simulations is devoted to the comparative study of the RMF-driven spin-up from a state of rest and the inertial spin-down following a short RMF pulse, corresponding to the time t_{on}, see Fig. 2(a). A comprehensive study considering the initial transient stage of an RMF-driven spin-up has recently been published by Nikrityuk et al. [30]. Their main findings are summarized only briefly here. If a spin-up is created by an RMF, the inviscid fluid starts to rotate due the azimuthal Lorentz force, and owing to the imbalance of the centrifugal forces and the pressure gradient forces in the near wall regions, a meridional flow is induced immediately. The first period of the spin-up process before the fluid has finished the first revolution around its own axis has been identified as the so-called *initial adjustment* (*i.a.*) phase, whose main features were described in Section 2.1. At the horizontal end walls Bödewadt-type boundary layers develop. Inside these layers the liquid flows radially inwards carrying fluid with the angular momentum $u_\theta r$ from the large radii towards the cylinder axis. The corresponding increase in angular velocity Ω in the Bödewadt layer generates new vortices appearing near the endwalls. In this way, the boundary layer develops into a multi-layered structure during a short period of time. In the range of magnetic Taylor numbers considered here the side wall layers also become unstable, resulting in the appearance of Taylor–Görtler vortices.

Now we compare the fluid dynamics during the spin-up[1] and the spin-down after the RMF pulse. The initial condition of the classic spin-down is always an ideal solid-body rotation of the liquid with the cylinder which is characterized by the absence of a meridional flow. By contrast, the flow structure set up during the RMF-driven spin-up is transient, and the fully-developed flow field is turbulent for $Ta > Ta_{\text{cr}}^{\text{3D}}$. To start the spin-down process in our case, a well-defined and reproducible initial condition is necessary at which the magnetic field is switched off. A natural choice is the moment just after completion of the initial adjustment phase, i.e. $t = t_{\text{ia}}$ for two reasons. First, the underlying flow structure at that time is the same for all Ta [28,30]. Second, the ratio between secondary to primary flow velocity reaches a maximum at that point [30], making this event attractive for mixing strategies. Switching off the RMF at that instant is equivalent to the application of an RMF pulse with a defined pulse length, t_{on}, covering the duration of the initial adjustment phase.

In order to analyse the temporal evolution of the global flow field, the volume-averaged meridional (Eq. (6)) and azimuthal velocities have been introduced:

$$U_\theta = \frac{2}{R_0^2 H_0} \int_0^{H_0} \int_0^{R_0} r u_\theta \, dr \, dz. \tag{11}$$

The resulting histories for both the spin-up and the RMF pulse (pulse length $t_{\text{on}} = t_{\text{ia}}$) are depicted in Fig. 3 for different magnetic Taylor numbers. Following Nikrityuk et al. [30] Figs. 3(a) and 3(b) are plotted vs nondimensional times $t' = t/t_{\text{spin-up}}$ and $t'' = t/t_{\text{ref}}$, respectively. Note that the physical time t is the same in Figs. 3(a) and 3(b), i.e. $t = t' \cdot t_{\text{spin-up}} = t'' \cdot t_{\text{ref}}$. From Fig. 3(a) it can be seen that with an increase in Ta the braking rate of the primary flow ($\partial U'_\theta / \partial t < 0$) increases after completion of the RMF pulse.

The analysis of Fig. 3(b) shows similar sinusoidal oscillations of U_{rz} for both the continuous spin-up and the spin-down after the RMF pulse. These oscillations are fingerprints of inertial waves [3,12,17,30] which propagate from the horizontal end walls towards the midplane. They are discussed in more detail with the next figures. The characters **A**, **B** and **C** in Fig. 3(b) denominate the particular local maxima and minima in U_{rz} during the RMF pulse for $Ta = 2.65 \times 10^6$. It is important to note that the spin-up and spin-down curves at each given Taylor number proceed in close relation until the first minimum, see characters **A** and **B**. The positions of later maxima and minima then reveal a particular time shift.

In Figs. 4 and 5 we plot the snapshots of the fluid flow for $Ta = 2.65 \times 10^6$ corresponding to the maxima or minima in U_{rz}. Until the end of the *i.a.* phase (Fig. 4(a)) the secondary flow develops in the form of two toroidal vortices which are symmetrical with respect to the midplane of the cylinder. The dynamic formation of the Bödewadt layer during spin-up takes place in the time interval between points **A** and **B**, cf. Figs. 4(b)–(d). The multi-layered structure of the horizontal boundary layers is clearly visible in Fig. 4(d). The development of this structure is attributed to the radial outflow parallel to the end walls which brakes the azimuthal flow through the term $u_r u_\theta / r$ and thus causes the

[1] Here and further in the text the spin-up means the acceleration of the fluid flow driven by RMF pulse of *infinite* length.

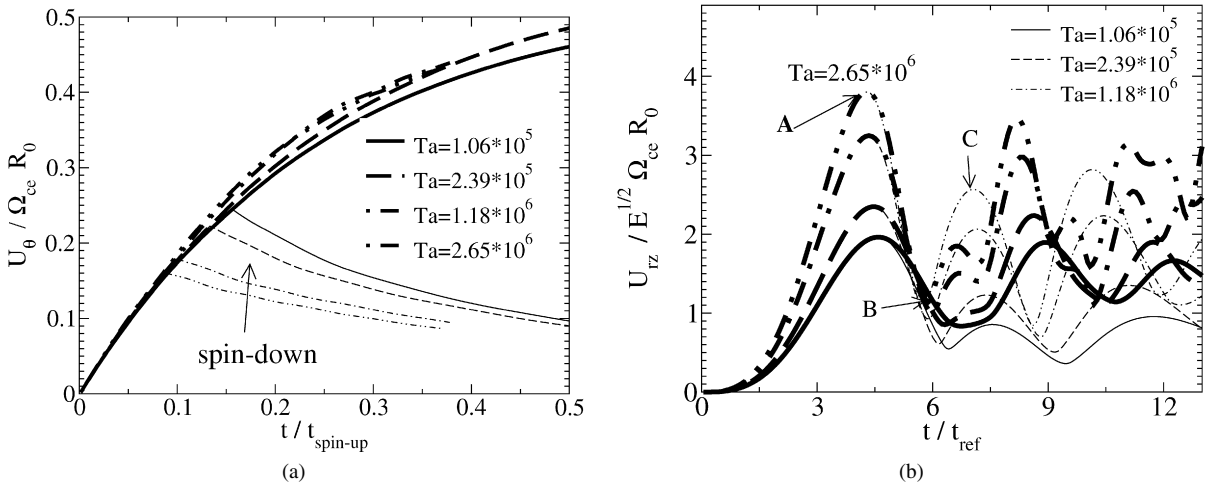

Fig. 3. Time history of the volume-averaged azimuthal velocity, U'_θ (a) and meridional velocity, U'_{rz} (b). Thick and thin lines correspond to the spin-up and spin-down, respectively. The prime ($'$) denotes the dimensionless variables with respect to the scaling (10). The characters **A**, **B** and **C** denominate the particular local maxima and minima in U_{rz} during RMF pulse for $Ta = 2.65 \times 10^6$.

change in the axial gradient of u_θ. To compare the evolution of the fluid flow after the RMF pulse, in Figs. 5(a)–(b) we show the snapshots for the same times as for spin-up. It can be seen that despite a decrease in the volume-averaged azimuthal velocity, the plots of the secondary flow pattern in Figs. 4(b)–(d) and 5(a)–(c) show a clear similarity until the first minimum, point **B**. After that instant, the difference between continuous spin-up and spin-down after the RMF pulse becomes obvious. In particular, as spin-down progresses, the thickness of the side wall layer on the midplane of the cylinder increases due to the friction force. Accordingly Fig. 5(d) shows the flow corresponding to the 2nd maximum of U_{rz}, see point **C** in Fig. 3(b).

We note that in spite of a different quantitative behavior of U_{rz} for the spin-up and RMF pulse after point **B**, *all* local maxima in U_{rz} for both cases always show a meridional flow structure dominated by a pair of counter-rotating vortices. The difference consists in the direction of rotation of these vortices. In particular, the comparison of the flow pattern at the first maximum of U_{rz} during spin-up, point **A**, and the second maximum of U_{rz} during the RMF pulse, point **C**, reveals a reversal of the flow direction, see Figs. 4(a) and 5(d). The explanation of this type of oscillatory recirculation was given by Davidson [16], who showed that any axial gradient in a swirl acts as a source of meridional recirculation, which, in turn, affects the azimuthal velocity itself. This interaction of the primary and secondary flow takes place via inertial waves. In the context of RMF-driven fluids [17,30] the period of these waves in a developed regime can be described quite well by

$$T_{\text{class}} = \frac{\pi}{\Omega_{\text{ce}}}\left[1 + \left(\xi_1 \frac{H_0}{2R_0\pi}\right)^2\right]^{1/2} \tag{12}$$

as known from the classic analysis (Greenspan [3], Section 2.5) for an axisymmetric inertial eigenmode ($k = 0$, $n = 2$, $m = 1$). $\xi_1 = 3.83$ is the first positive root of the corresponding Bessel function [30]. To give an example, for $\Omega_{\text{ce}} = 4.51\ \text{s}^{-1}$ (cf. Table 1) the eigenperiod is $T_{\text{class}} = 1.1$ s. During spin-up the liquid angular velocity Ω increases with time, which results in a decrease in the eigenperiod of the inertial waves. We found that at the beginning of spin-up the eigenperiod takes about $3T_{\text{class}}$. The opposite behavior is observed during spin-down. Here, the eigenperiod of the first inertial waves is about 2–2.5T_{class} and increases at decreasing amplitudes. During the start of the spin-down we could clearly identify the solitary inertial wave as described by Valentine and Miller [12] for the classic spin-down. Further undulation of flow structures along the axis of the cylinder can be observed between the maxima and the minima in the temporal behavior of U_{rz}.

Fig. 6 shows the ratio between the volume-averaged meridional and the volume-averaged azimuthal velocity. It can be seen that in the case of the RMF pulse the absolute value of U_{rz}/U_θ clearly exceeds the analogue quantity for the spin-up. Recently, however, it was shown that a periodical switching on and off of the RMF keeps the same magnitude of meridional velocities at a distinctly lower level of the swirl flow [41]. As we have applications in mind where an

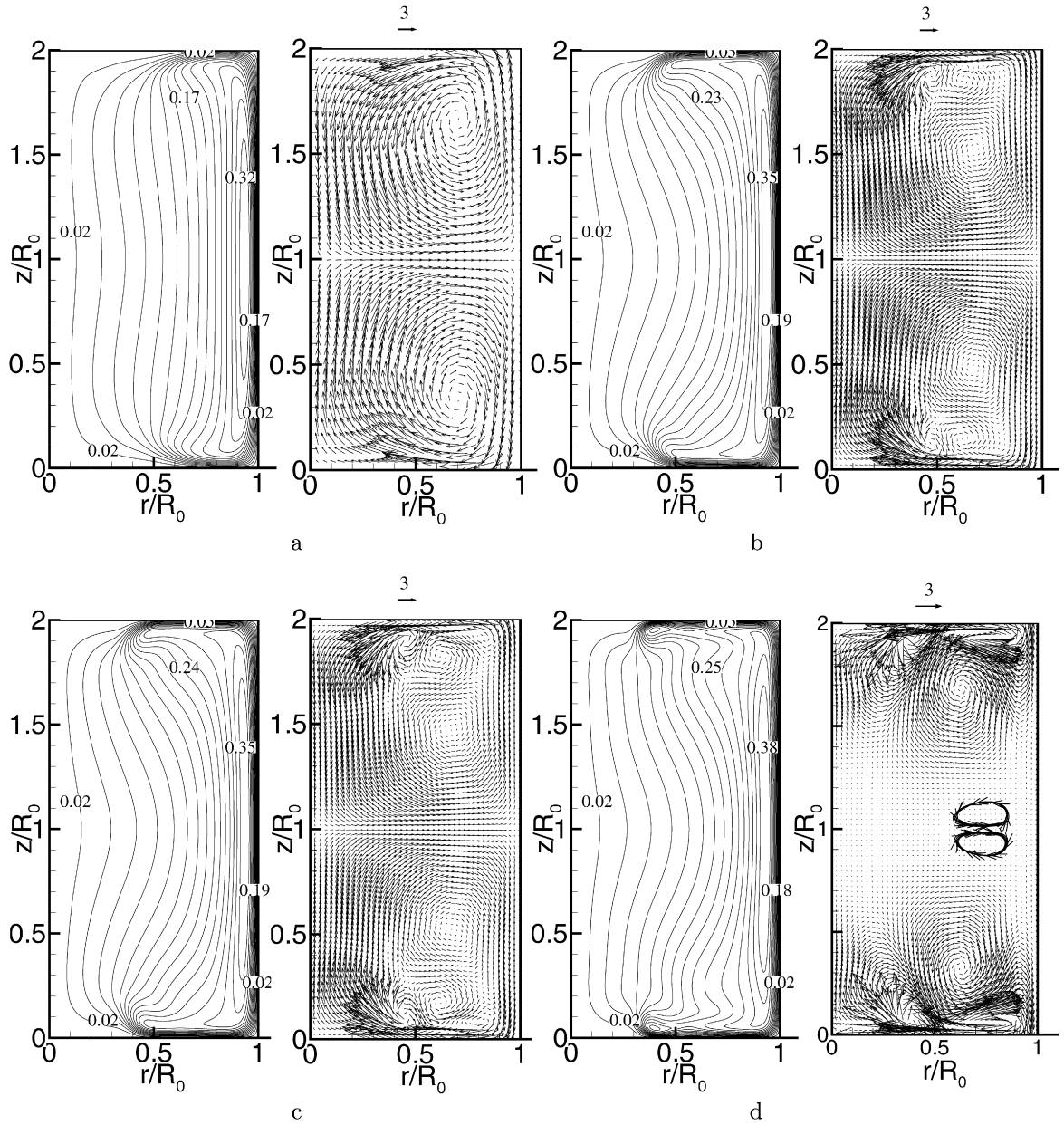

Fig. 4. Flow structures for different times during *spin-up* at $Ta = 2.65 \times 10^6$ (contour plots for u'_θ left, vector plots for u'_r and u'_z right, every 4th vector is shown). (a) $t/t_{\text{ref}} = 4.31$ – initial adjustment phase, see letter **A** in Fig. 3(b); (b) $t/t_{\text{ref}} = 5.19$; (c) $t/t_{\text{ref}} = 5.31$; (d) $t/t_{\text{ref}} = 5.88$ – inertial phase, first minimum in U'_{rz}, see letter **B**.

effective mixing shall be provided by the secondary flow, a periodical modulation of the RMF could be an efficient, energy-saving tool.

5.2. Cylinder with free surface: dynamics of the flow driven by RMF pulses of variable length

5.2.1. Comparison between enclosed and free surface cylinders

To demonstrate the robustness of our findings we now move from the mid-plane symmetric closed cylinder to a mid-plane non-symmetric case. This is the cylinder with a free surface, which is also important for practical applications, e.g. in metallurgy. To explore the difference between the fluid flow in both cavities and to check if the scaling

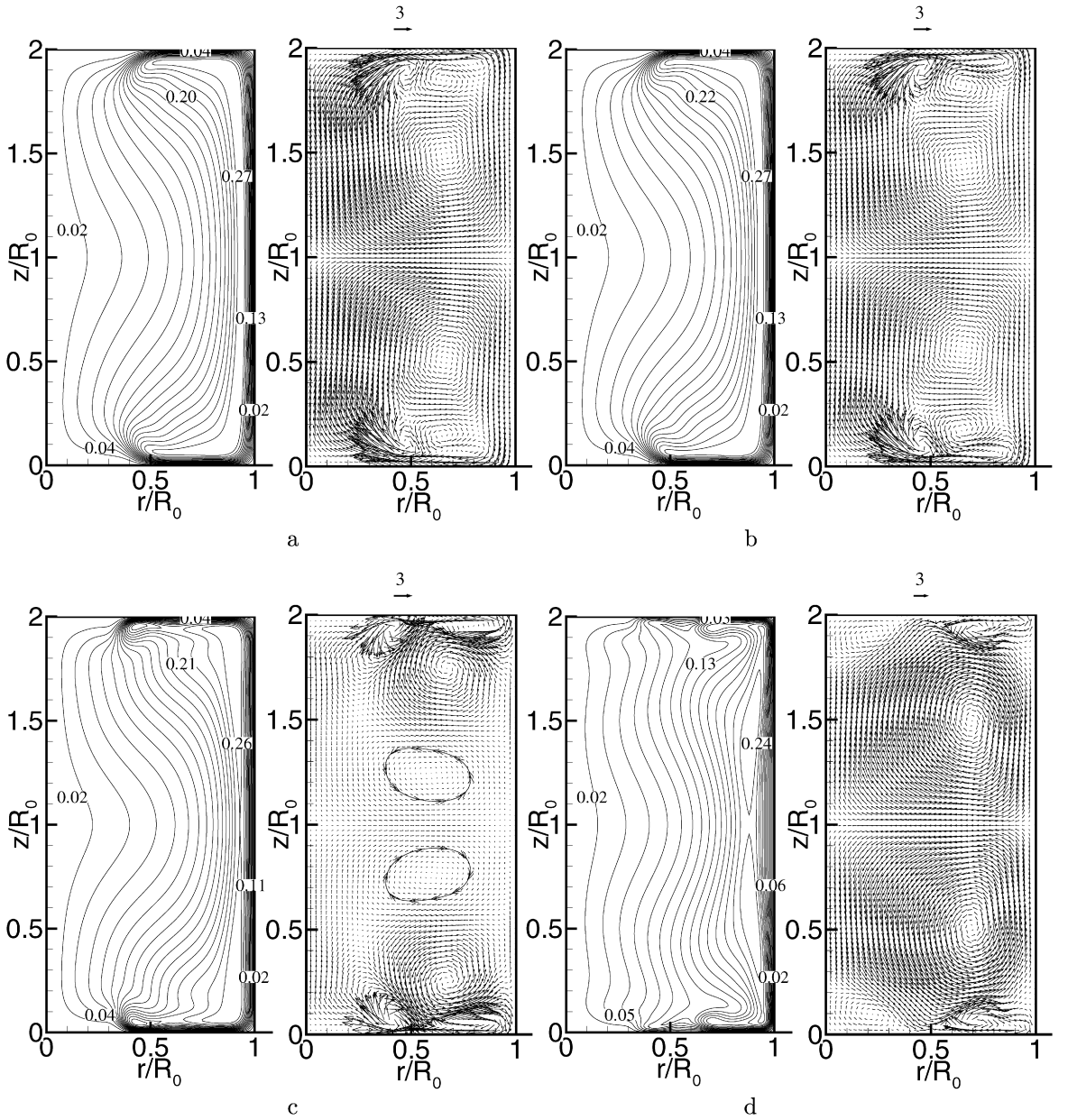

Fig. 5. Flow structures for different times during *spin-down* at $Ta = 2.65 \times 10^6$ (contour plots for u'_θ left, vector plots for u'_r and u'_z right, every 4th vector is shown). (a) $t/t_{\text{ref}} = 5.19$; (b) $t/t_{\text{ref}} = 5.31$; (c) $t/t_{\text{ref}} = 5.75$ – "solitary" wave phase, first minimum in U'_{rz} during spin-down, see letter **B** in Fig. 3(b); (d) $t/t_{\text{ref}} = 7.06$ – 2nd maximum in U'_{rz} during spin-down, letter **C** in Fig. 3(b).

parameters used for an enclosed cavity, see Eq. (10), are correct for a free surface, we first compare the dimensionless time required for the flow to reach the steady state for $Ta < Ta_{\text{cr}}^{\text{3D}}$ and the unsteady developed regime for $Ta > Ta_{\text{cr}}^{\text{3D}}$. The computations were performed for cylindrical containers of aspect ratio A equal to 1 for $Ta = 1.06 \times 10^5$ and $Ta = 2 \times 10^6$. Following Nikrityuk et al. [30] we define the time required for the flow to become fully developed, $\tau_{\text{dev}} = t_{\text{dev}}/t_{\text{spin-up}}$, by using the volume-averaged azimuthal velocity U_θ. Its time history is shown Fig. 7(a). It can be seen that the curves obtained for the closed and the free surface cylinders for both Ta collapse to one line and asymptotically reaches the values 0.52 and 0.65, respectively. Based on the procedure described in Ref. [30] we found that for the closed cylinder $\tau_{\text{dev}}^{\text{closed}} = 1.1$ and for the free surface cylinder $\tau_{\text{dev}}^{\text{free}} = 1.35$. The ratio between both times is 1.23. Thus the angular velocity scaling using Ω_{ce} is also correct for a free surface. This finding is supported by a

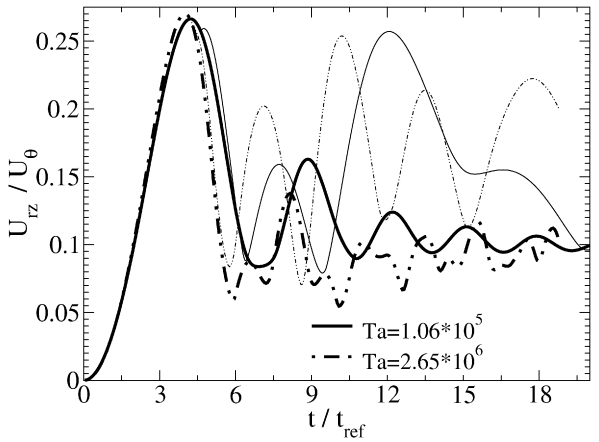

Fig. 6. Time history of the ratio between volume-averaged meridional to azimuthal velocity. Thick lines refer to spin-up, thin lines refer to spin-down.

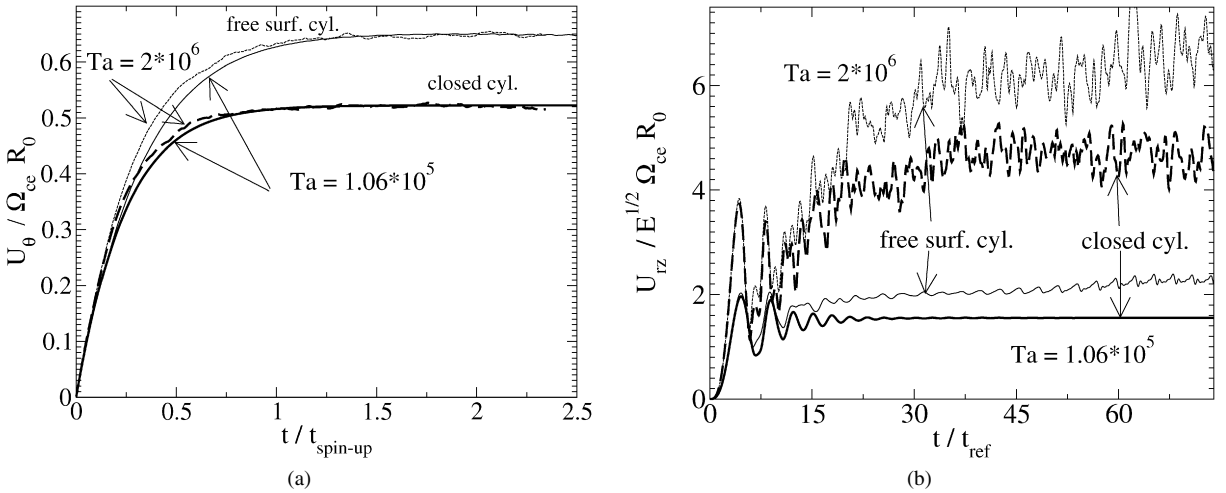

Fig. 7. Time history of the volume-averaged azimuthal velocity, U'_θ (a) and nondimensional volume-averaged meridional velocity, U'_{rz} (b) during continuous spin-up calculated for different Ta and $A = 1$. Thick and thin lines correspond to the closed cylinder and the cylinder with the free surface, respectively. The prime ($'$) denotes the dimensionless variables with respect to the scaling (10).

comparison of the time-averaged angular velocity and meridional flow vector plots shown in Fig. 8. It can be seen that the ratio of the angular velocities of the core, $\Omega^{\text{free}}/\Omega^{\text{closed}}$ is about 1.5. The same is true for the ratio of the velocities of the meridional flow.

The analysis of the time histories of the volume-averaged meridional velocity, U_{rz} shown in Fig. 7(b), doubtless proves that the duration of the initial adjustment phase, t_{ia}, is identical for the closed and as well as for the free surface cavity. To be precise, for $Ta = 1.06 \times 10^5$ and $Ta = 2 \times 10^6$ we found $t_{\text{ia}}/t_{\text{ref}} = 4.6$ and $t_{\text{ia}}/t_{\text{ref}} = 4.33$, respectively.

5.2.2. The influence of the RMF pulse length

In this section we study the impact of different RMF pulse lengths on the fluid flow in a cylinder with free surface. In particular we present a comparison between the numerical calculations and corresponding experimental results focused on the secondary flow. All experimental results rely on profiles of the vertical velocity measured at a radial position of $r/R_0 = 0.6$ parallel to the cylinder axis. The magnetic field strength was adjusted to 2.69 mT corresponding to a Taylor number of 4.17×10^6, which provides the following scaling parameters: $t_{\text{ref}} = 0.92$ s, $t_{\text{ia}} = 3.95$, $t_{\text{spin-up}} = 49.83$ s, $\Omega_{\text{ce}} = 4.26$ 1/s and $E_{\text{ce}} = 8.86 \times 10^{-5}$. The time scales to accomplish the initial adjustment phase were calculated to be $t_{\text{ia}}/t_{\text{ref}} = 4.29$ and $t_{\text{ia}}/t_{\text{spin-up}} = 0.08$.

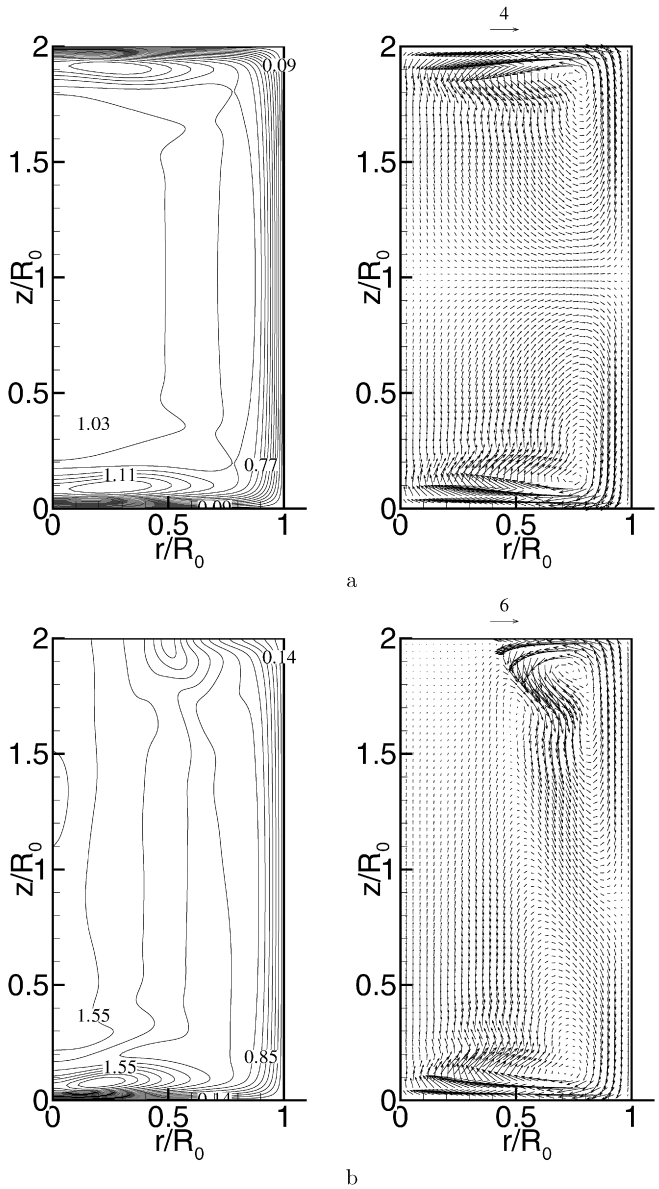

Fig. 8. Time-averaged flow structures for the closed cylinder (a) and the cavity with the free surface (b) calculated for $Ta = 1.06 \times 10^5$ (contour plots for Ω' left, vector plots for u'_r and u'_z right, every 4th vector is shown).

In contrast to Section 5.1 we additionally vary the pulse durations between $t_{on}/t_{ia} = 0.66$ ($t_{on}/t_{ref} = 2.83$) and 2.53 ($t_{on}/t_{ref} = 10.87$), corresponding to 2.6 s and 10.0 s, respectively. Fig. 9 shows the volume-averaged azimuthal and secondary flow velocities, U_θ and U_{rz}, thereby comparing the RMF pulses with the situation of the corresponding spin-up at the same Taylor number. As already shown for the enclosed cylinder all U_{rz} curves reach the first local maximum at about the same time, see Fig. 9(b). The numerical results demonstrate that U_{rz} undergoes inertial oscillations of the same type as already described for the enclosed cylinder. On the other hand, an increase on t_{on} increases the number of oscillations and reduces their eigenperiod. This can be explained by the higher value of the angular velocity at the moment when the RMF is switched off. The diagram contains the square value of the vertical velocity component averaged along a vertical line at a radial measuring position of $r/R_0 = 0.6$. Fig. 10 confirms the finding that the *i.a.* phase is completed at about the same time for all t_{on}.

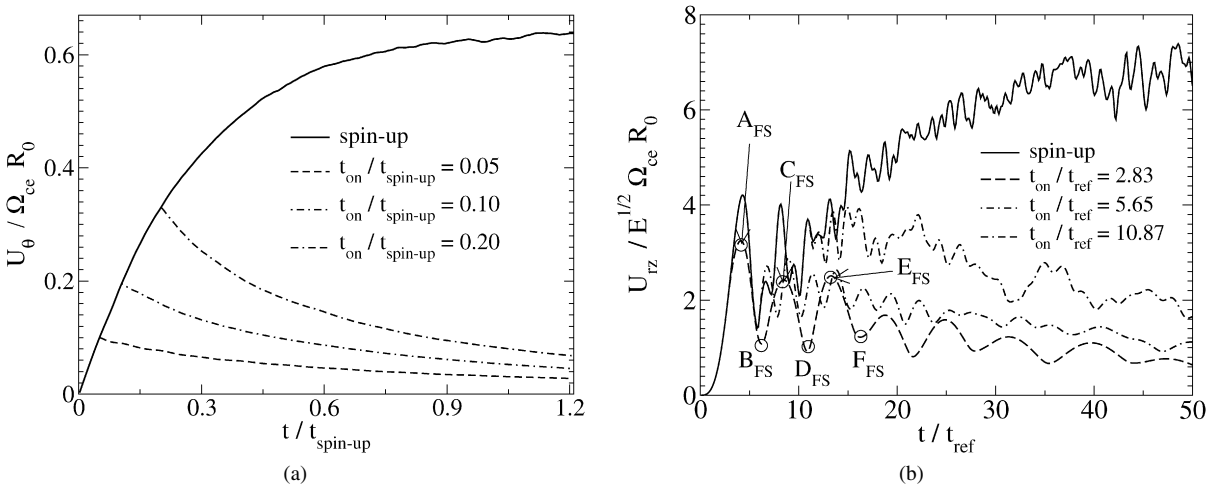

Fig. 9. Time history of the volume-averaged azimuthal (a) and meridional velocity (b) calculated for the cylinder with free surface, $Ta = 4.17 \times 10^6$, $A = 1$. Here the letters $\mathbf{A_{FS}} \ldots \mathbf{F_{FS}}$ depict the local maxima and minima of U_{rz} for $t_{\mathrm{on}}/t_{\mathrm{ref}} = 2.83$ ($t_{\mathrm{on}}/t_{\mathrm{ia}} = 0.66$).

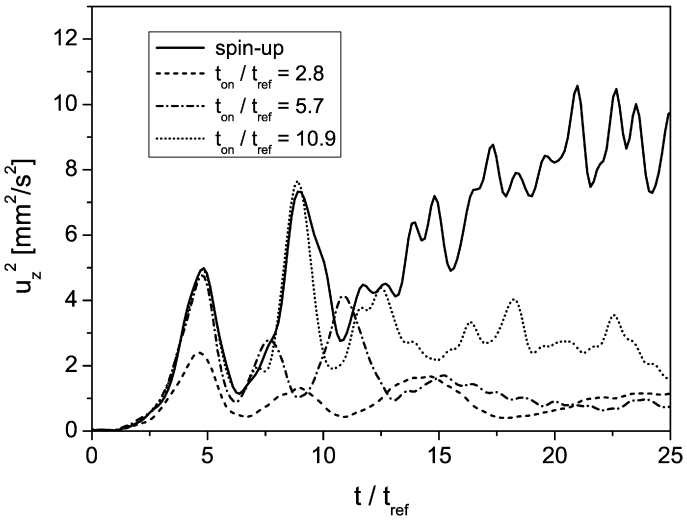

Fig. 10. Time history of the squared axial velocity averaged along the height of the cylinder at $r/R_0 = 0.6$. Experimental results.

Details of the meridional flow pattern for $t_{\mathrm{on}}/t_{\mathrm{ia}} = 0.66$ ($t_{\mathrm{on}}/t_{\mathrm{ref}} = 2.83$) are presented in Fig. 11 at the moment when the volume-averaged flow U_{rz} passes the first three local maxima and minima, respectively, as shown in Fig. 9(b). The letters $\mathbf{A_{FS}} \ldots \mathbf{F_{FS}}$ depict these local maxima and minima for $t_{\mathrm{on}}/t_{\mathrm{ia}} = 0.66$. We found that the pertinent flow patterns resulting from a pulse length $t_{\mathrm{on}} \leqslant t_{\mathrm{ia}}$ are very similar. Fig. 11(a) (point $\mathbf{A_{FS}}$ in Fig. 9(b)) reveals the flow structure after end of the initial adjustment phase. During spin-down the fluid experiences inertial oscillations leading to a restructuring of the flow. Owing to the friction force at the end walls the modification of the flow emanates from the Bödewadt layer and the free surface. Fig. 11(b) shows a snapshot at the time corresponding to the first minimum in U_{rz} (point $\mathbf{B_{FS}}$ in Fig.9(b)). The double-vortex structure known from the initial adjustment phase has been transformed into rather strong vortices close to both horizontal boundaries. Between these outer vortices, four new vortices appear. The intensity of the vortices near the midplane of the cylinder is very low. In the further course of the process the pattern of the six toroidal vortices is again replaced by a structure dominated by a double-vortex as displayed in Fig. 11(c), point $\mathbf{C_{FS}}$ in Fig. 9(b). These snapshots coincide with the second maximum in U_{rz}. It is worth pointing out that compared to the first maximum of U_{rz} these vortices show a reversed direction of rotation. Furthermore, two small vortices occur along the horizontal boundaries of the cylinder. This multilayer flow structure can also be detected in

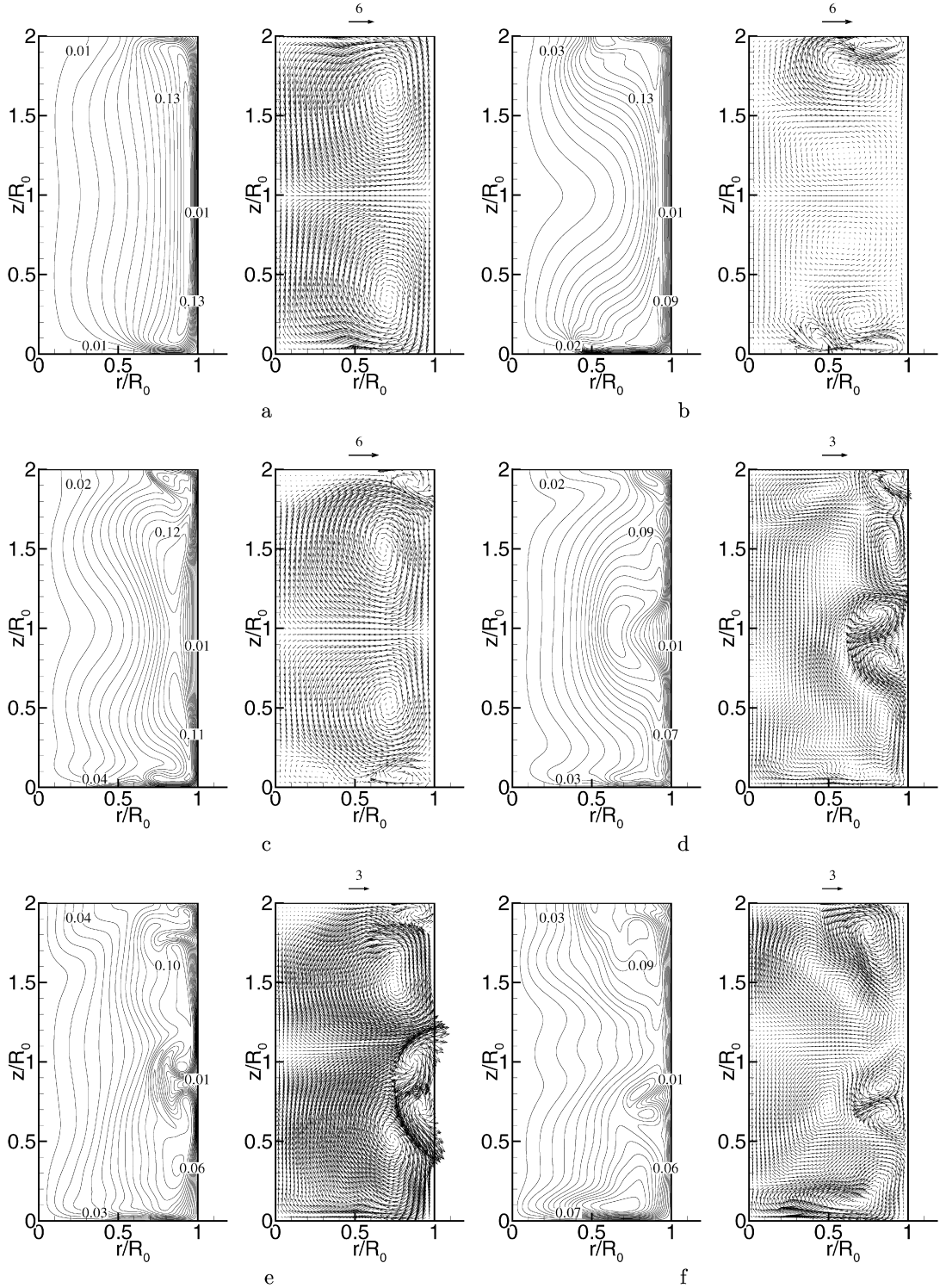

Fig. 11. Flow structures in a cylinder with free surface during a *short* RMF pulse ($t_{on}/t_{ref} = 2.83$ or $t_{on}/t_{ia} = 0.66$) at $Ta = 4.17 \times 10^6$ (contour plots for u'_θ left, vector plots for u'_r and u'_z right, every 4th vector is shown): (a) $t/t_{ref} = 4.24$ – first maximum in U'_{rz}, point $\mathbf{A_{FS}}$, see Fig. 9(b); (b) $t/t_{ref} = 6.20$ – first minimum in U'_{rz}, point $\mathbf{B_{FS}}$; (c) $t/t_{ref} = 8.48$ – second maximum in U'_{rz}, point $\mathbf{C_{FS}}$; (d) $t/t_{ref} = 10.87$ – second minimum in U'_{rz}, point $\mathbf{D_{FS}}$; (e) $t/t_{ref} = 13.30$ – third maximum in U'_{rz}, point $\mathbf{E_{FS}}$; (f) $t/t_{ref} = 16.30$ – third minimum in U'_{rz}, point $\mathbf{F_{FS}}$.

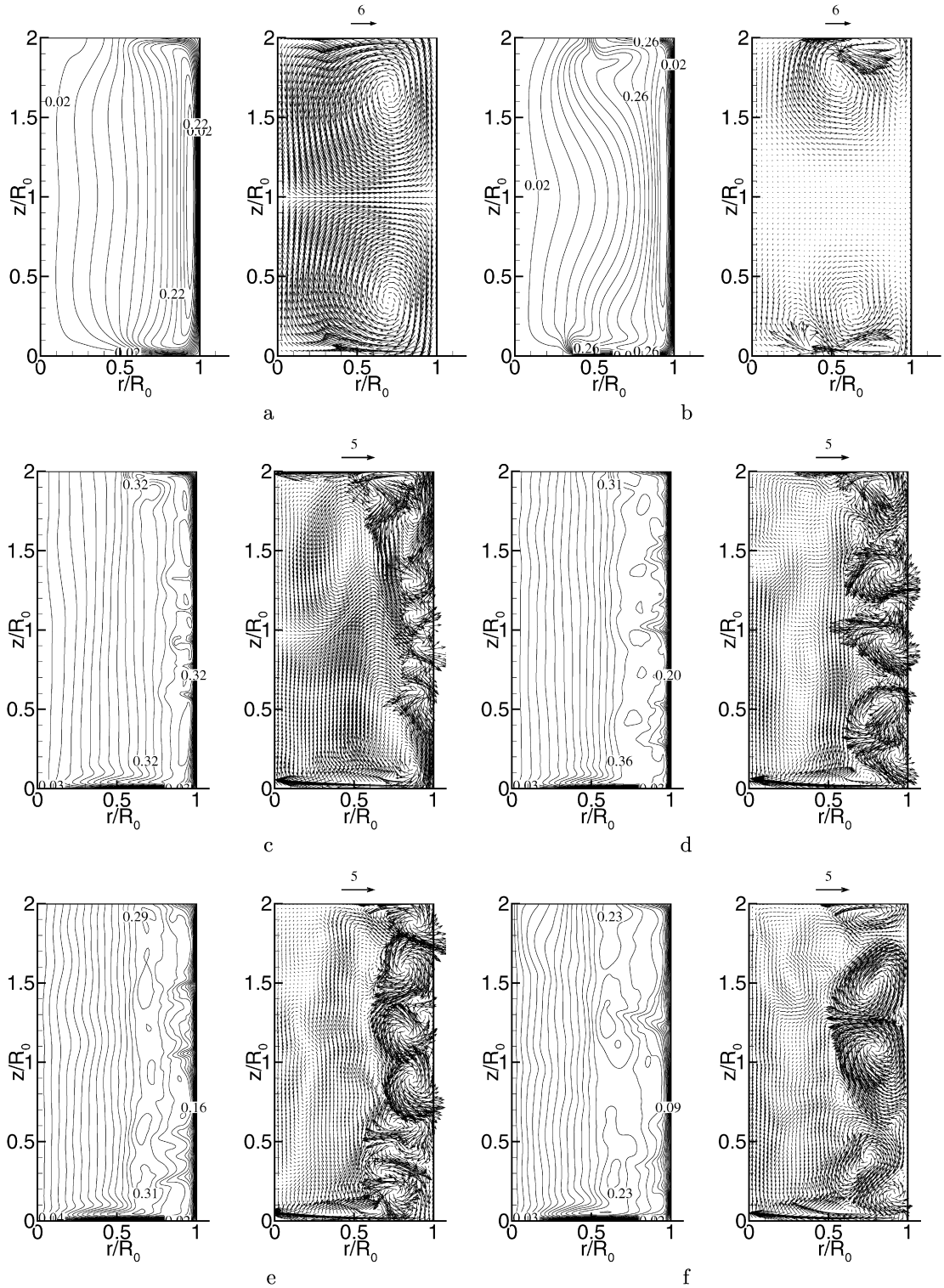

Fig. 12. Flow structures in a cylinder with free surface during a *long* RMF pulse ($t_{on}/t_{ref} = 10.87$ or $t_{on}/t_{ia} = 2.53$) at $Ta = 4.17 \times 10^6$ (contour plots for u'_θ left, vector plots for u'_r and u'_z right, every 3th vector is shown): (a) $t/t_{ref} = 4.29$ – first maximum in U'_{rz}; (b) $t/t_{ref} = 5.76$ – first minmum in U'_{rz}, see Fig. 9(b); (c) time averaged for $t/t_{ref} = 7.61$–10.90; (d) time averaged for $t/t_{ref} = 10.90$–16.30; (e) time averaged for $t/t_{ref} = 16.30$–21.70; (f) time averaged for $t/t_{ref} = 21.70$–32.60.

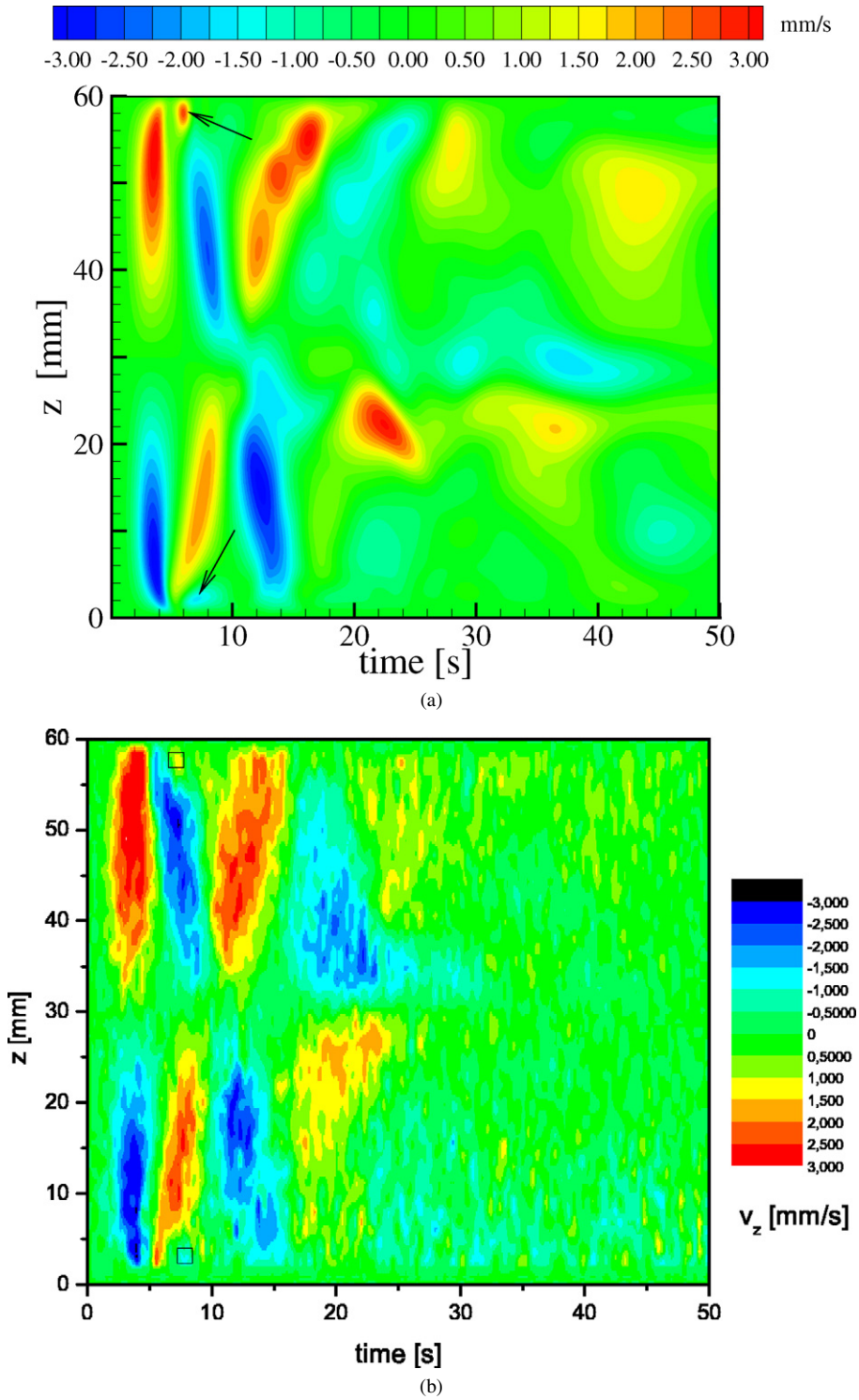

Fig. 13. Temporal development of the axial velocity along the height of the cylinder with free surface for $Ta = 4.17 \times 10^6$ and $t_{on} = 2.6$ s ($t_{on}/t_{ref} = 2.83$). (a) numerics, (b) experiment.

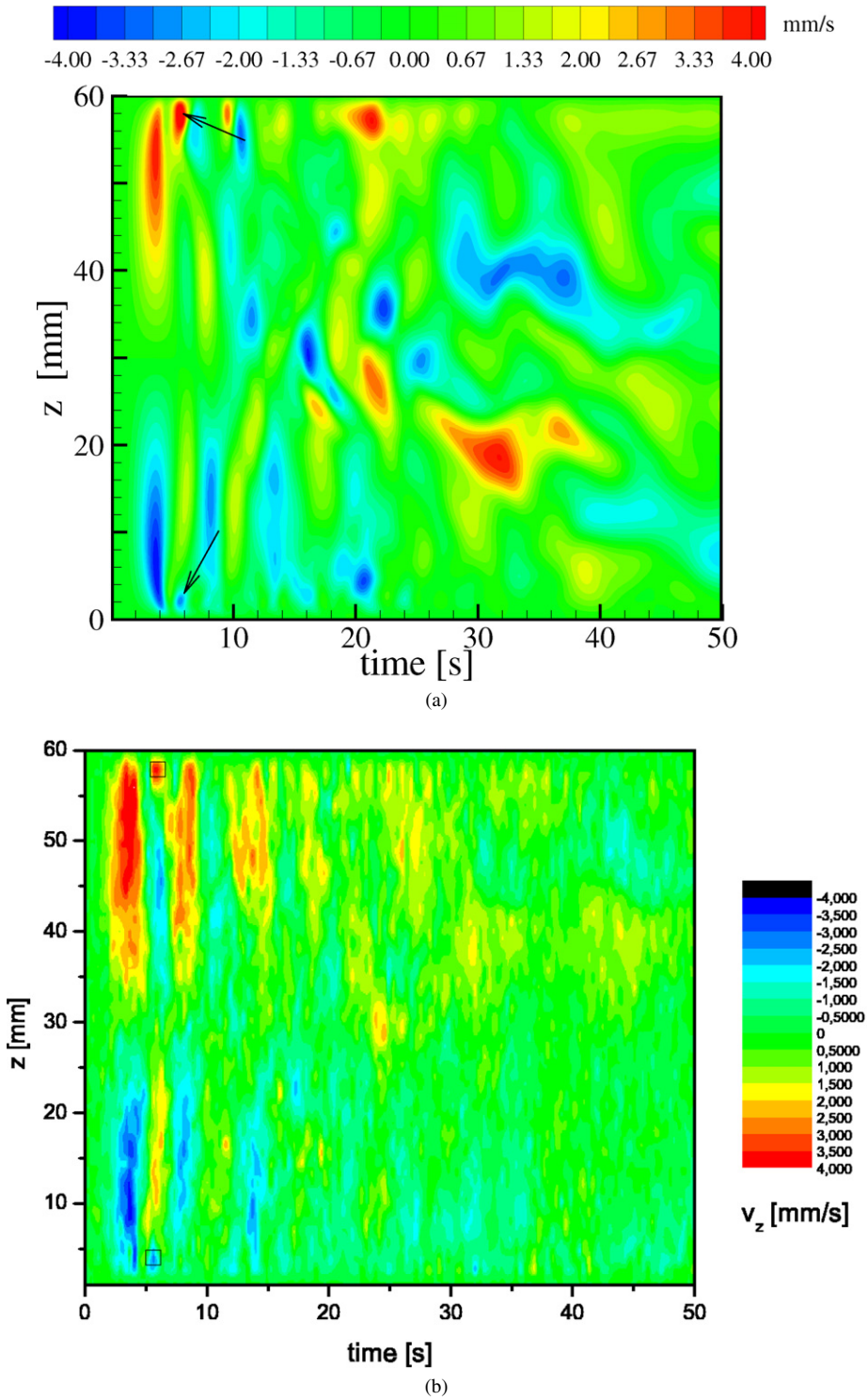

Fig. 14. Temporal development of the axial velocity along the height of the cylinder with a free surface for $Ta = 4.17 \times 10^6$ and $t_{on} = 5.6$ s ($t_{on}/t_{ref} = 5.65$). (a) numerics, (b) experiment.

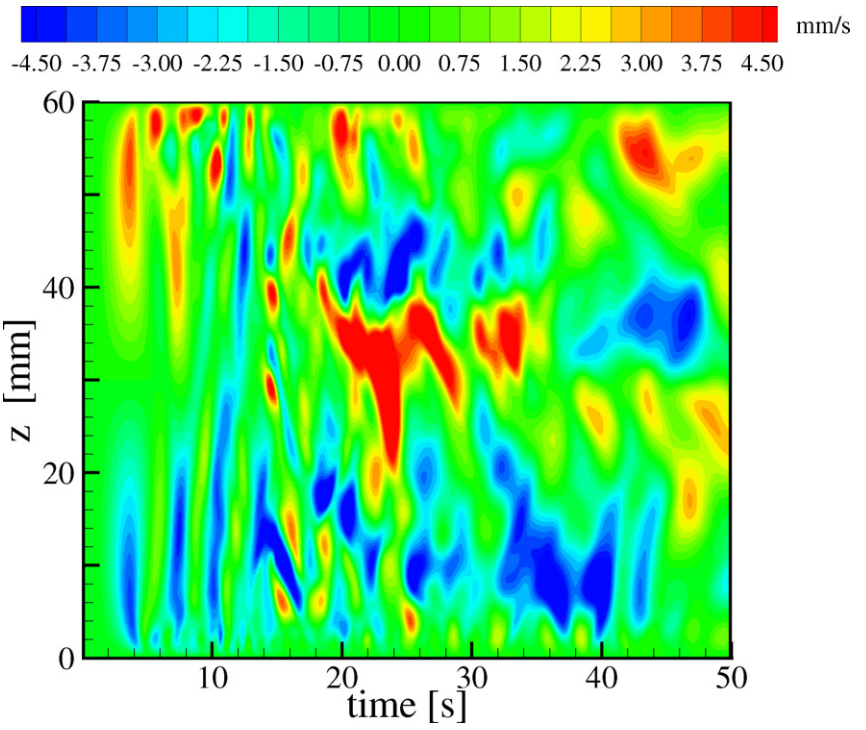

(a)

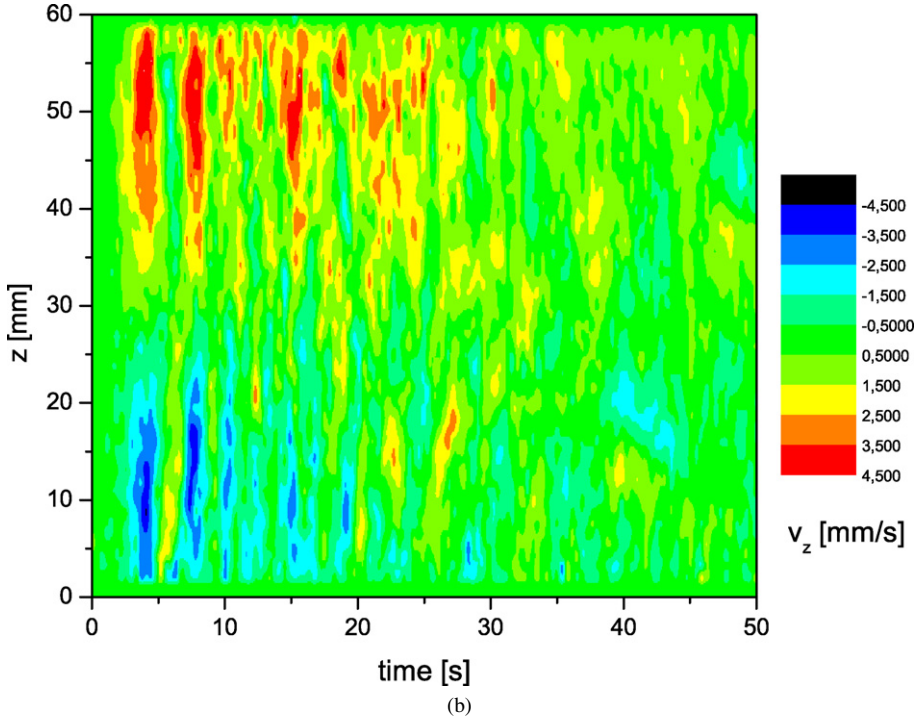

(b)

Fig. 15. Temporal development of the axial velocity along the height of the cylinder with a free surface for $Ta = 4.17 \times 10^6$ and $t_{on} = 10$ s ($t_{on}/t_{ref} = 10.87$). (a) numerics, (b) experiment.

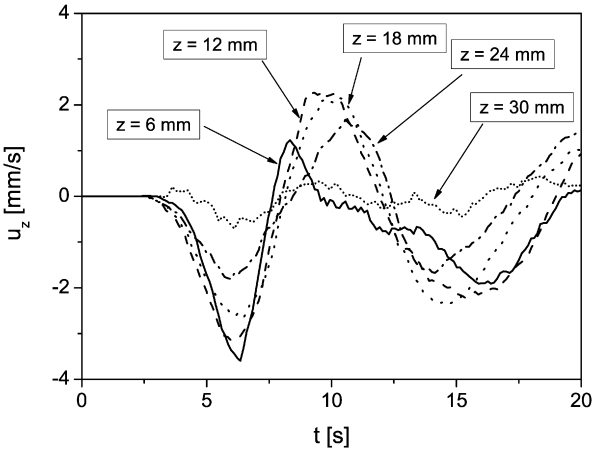

Fig. 16. Time history of the axial velocity obtained experimentally at different distances from the sensor for RMF pulse length of $t_{on}/t_{ref} = 2.8$.

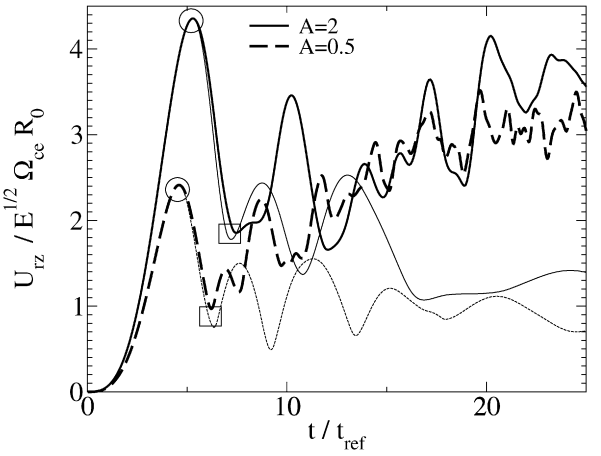

Fig. 17. Time history of the nondimensional volume-averaged meridional velocity calculated for different aspect ratios of the closed cavity for the same Ekman number $E_{ce} = 2.1 \times 10^{-4}$, which corresponds to $Ta = 9.32 \times 10^6$ ($A = 2$) and $Ta = 3.34 \times 10^5$ ($A = 0.5$). Thick and thin lines correspond to the spin-up and spin-down, respectively.

the experimental and numerical data marked by squares and arrows in Figs. 13 and 14 respectively, which will be presented below. Further braking of the flow is accomplished by the appearance of Taylor–Görtler vortices along the side walls of the cylinder and vortex breakdown near the axis of rotation, see Figs. 11(d) and 11(f) corresponding to the point $\mathbf{D_{FS}}$ and $\mathbf{F_{FS}}$ in Fig. 9(b). The third maximum in U_{rz} is related to a double-vortex structure almost the same as that already observed after the initial adjustment time, but at a lower intensity (see Fig. 11(e) corresponding to the point $\mathbf{E_{FS}}$ in Fig. 9(b)).

We found that in the case of pulse durations considerably longer than t_{ia} ($t_{on}/t_{ia} = 2.53$ or $t_{on}/t_{ref} = 10.87$) as shown in Fig. 12, we have a similar scenario of the meridional flow dynamics until the first minima of U_{rz} (Fig. 9(b)) as for the short RMF pulse ($t_{on}/t_{ia} = 0.66$), see Figs. 11(a)–(b) and 12(a)–(b). As time progresses, the flow pattern becomes more complex and dominated by smaller vortical structures such as the Taylor–Görtler (T–G) vortices appearing along the side wall, see Fig. 12(c). From this moment on, it makes sense to show time-averaged plots instead of snapshots because they display the global meridional flow. Fig. 12(c), for example, shows the flow pattern averaged over $t/t_{ref} = 7.61$–10.90, corresponding to the time before RMF was switched off at $t/t_{ref} = 10.87$. Figs. 12(d)–(f) depict the flow pattern after RMF was removed. The spin-down process in the case of a long RMF pulse is characterized by an increase in the size of T–G vortices.

Figs. 13, 14 and 15 show the temporal development of the flow field gained numerically and experimentally for the different pulse durations, which rely on profiles of u_z measured consecutively by means of UDV. In the graph the profiles are drawn along the ordinate, whereas the abscissa corresponds to the time axis. The bottom of the cylinder was defined as the zero point of the z coordinate. A positive velocity value corresponds to a descending flow. For a comparison between the experimental measurements and the numerical results, the spatial uncertainty of the measurements due to the finite size of the ultrasonic transducer was taken into account by spatial averaging of the numerical results as follows:

$$u_z^{\mathrm{UDV}}(z) = \frac{2\int_{R_1}^{R_2} u_z r\, dr}{R_2^2 - R_1^2}. \tag{13}$$

Here $R_2 - R_1$ is the thickness of the sensor. For our case R_1 and R_2 were set to 15.5 mm and 20.5 mm, respectively ($R_0 = 30$ mm). The spatio-temporal flow structures displayed in Figs. 13–15 reveal an excellent agreement between experiment and numerical simulation with respect to the temporal flow structure. At first a double vortex structure is established within the initial adjustment time of the spin-up. In the course of the process an alternating change of clockwise and counter-clockwise vortices can be observed. After the magnetic field is switched off the flow structure assumes the shape of an X. This finding clearly indicates the occurrence of a "solitary" wave propagating from each end wall towards the midplane of the cylinder as reported by Valentine and Miller [12]. This phenomenon also

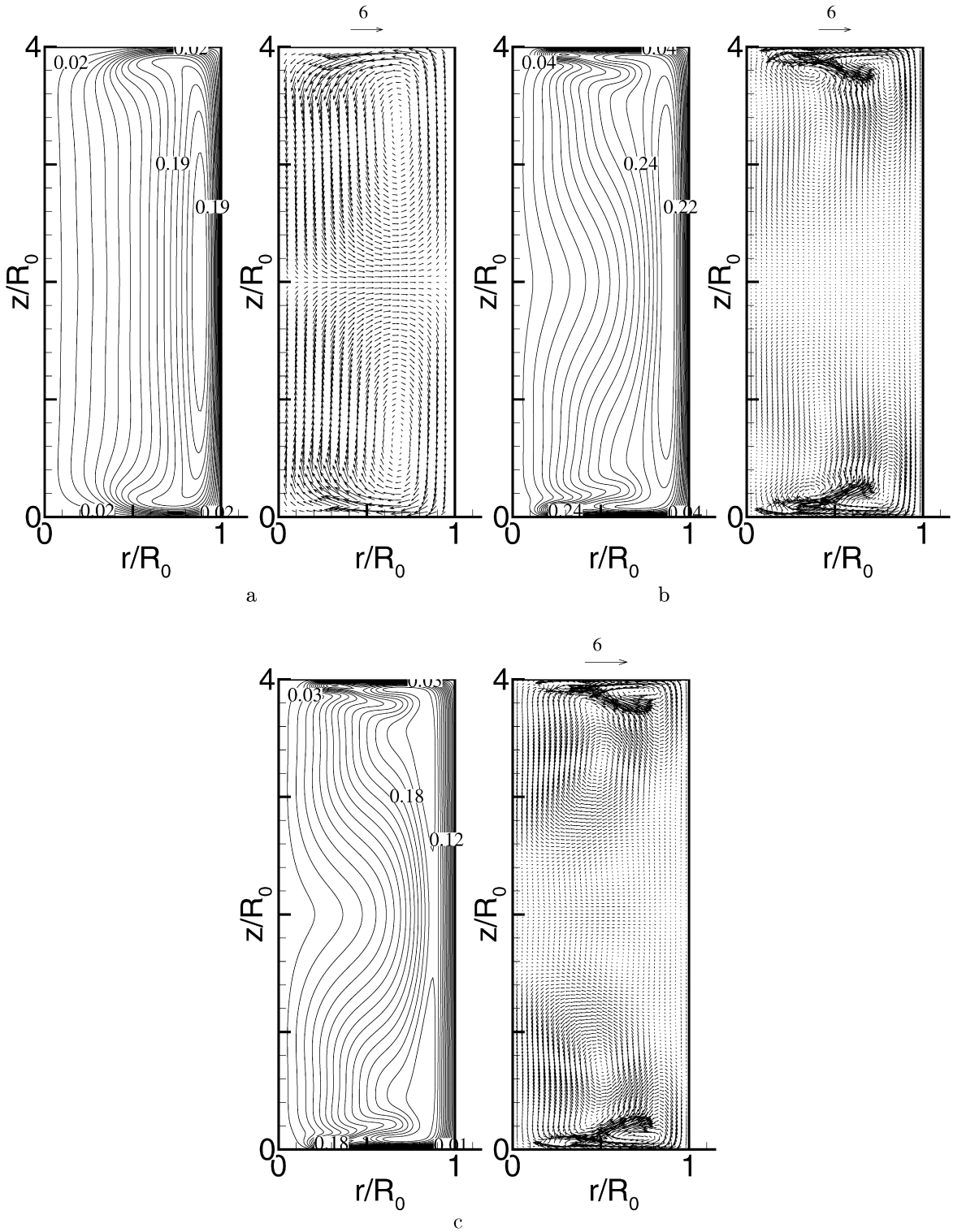

Fig. 18. Flow structures for different times during spin-up (a), (b) and spin-down (c) at $Ta = 3.34 \times 10^5$, $A = 0.5$ (contour plots for u'_θ left, vector plots for u'_r and u'_z right, every 4th vector is shown). Here (a) $t/t_{\text{ref}} = 4.6$, first maxima of U_{rz}, see Fig. 17; (b) $t/t_{\text{ref}} = 6.33$ (spin-up, first minima of U_{rz}, see Fig. 17); (c) $t/t_{\text{ref}} = 6.33$ (spin-down, first minima of U_{rz}, see Fig. 17).

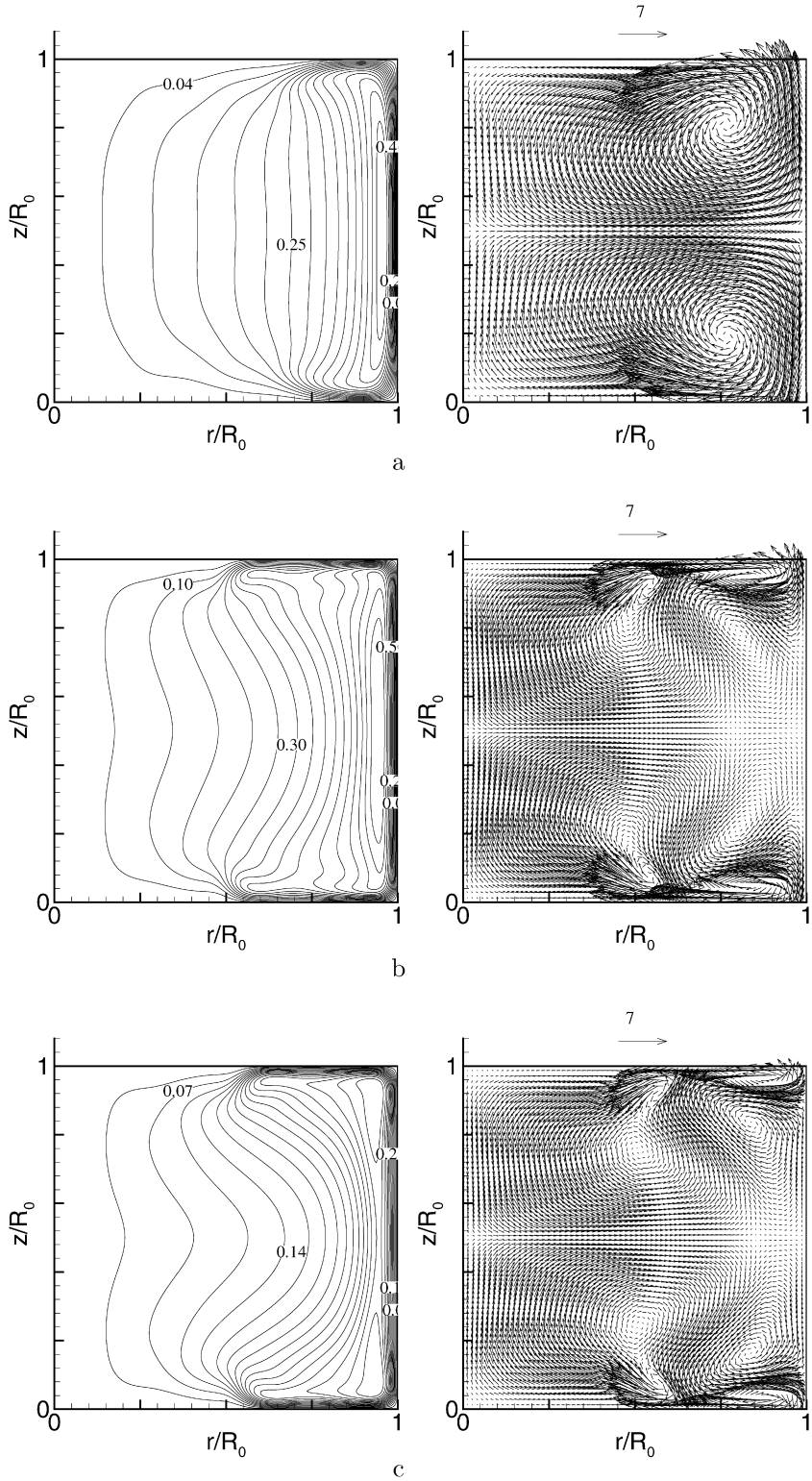

Fig. 19. Flow structures for different times during spin-up (a), (b) and spin-down (c) at $Ta = 9.32 \times 10^6$, $A = 2$. Here (a) $t/t_{\text{ref}} = 5.3$, first maxima of U_{rz}, see Fig. 17; (b) $t/t_{\text{ref}} = 7.5$ (spin-up, first minima of U_{rz}, see Fig. 17); (c) $t/t_{\text{ref}} = 7.2$ (spin-down, first minima of U_{rz}, see Fig. 17).

becomes visible if the time series of the velocity are analyzed for different vertical positions as can be seen in Fig. 16 for a pulse length of $t_{on}/t_{ref} = 2.83$ ($t_{on}/t_{ia} = 0.66$). Whereas the initial double vortex appears at the same moment for all positions, the following counter-rotating vortex arrives later the farther the position is away from the end walls. From Figs. 13–15 it also becomes apparent that the wave moves faster when the RMF pulse duration is longer. For a variation between $t_{on}/t_{ref} = 2$ and $t_{on}/t_{ref} = 12$ the velocity of propagation increases from about 3 mm/s to 10 mm/s.

However, the spatio-temporal plots of the velocity field also reveal deviations between experimental and numerical results after RMF is removed at $t_{on}/t_{ref} = 10.87$ ($t_{on}/t_{ia} = 2.53$). This might be an indication that the assumption of an axisymmetric flow field fails. Another question arises with respect to the impact of the ultrasonic sensor, which is immersed into the liquid only a few mm below the free surface. Although all measurements were repeated several times to prove the reproducibility of the data, it cannot be definitely excluded that to some extent the measurement itself provokes flow perturbations. This problem will be tackled in future by further experiments using an enclosed fluid container.

6. Conclusions

The issue of the present paper is the evolution of the flow structure inside a cylindrical liquid metal column exposed to a single rotating magnetic field pulse. The results show that the secondary flow in the r–z plane undergoes periodic inertial oscillations during spin-up and spin-down. We found that each local maximum of the volume-averaged meridional velocity U_{rz} is related to a flow pattern dominated by a double vortex, whereby the vortices change their sense of rotation between two consecutive maxima. This finding is irrespective of whether the cylinder has a non-slip or a slippery upper wall. The analysis of the transient dynamics of the flow after the RMF pulse shows similarities between the meridional flow pattern until the first local minimum of U_{rz}. We found especially that an RMF pulse with a duration equal to the initial adjustment time triggers a very harmonic oscillatory recirculation. This type of motion can be considered as an efficient tool to enhance heat and mass transfer, desired during solidification processes, for example. The analysis of sequences of RMF pulses is the subject of a work in progress.

Acknowledgements

The financial support by the Deutsche Forschungsgemeinschaft as part of the SFB 609 "Electromagnetic flow control in metallurgy, crystal growth and electrochemistry" is gratefully acknowledged. The authors also would like to express their thanks to D. Räbiger for his valuable support in preparing and performing the experiments.

Appendix A

In this appendix we would like to demonstrate that the distinct similarity in the secondary flow pattern between spin-up and spin-down after the RMF pulse is universal and not restricted to aspect ratios equal to unity. For this purpose the volume-averaged meridional velocity U_{rz} has been calculated for the aspect ratios $A = 2$ and $A = 0.5$ at the same Ekman number $E_{ce} = 2.1 \times 10^{-4}$, which corresponds to $Ta = 9.32 \times 10^6$ ($A = 2$) and $Ta = 3.34 \times 10^5$ ($A = 0.5$), see Fig. 17. In the case of the RMF pulse (thin line) the RMF is switched off when U_{rz} reaches the first maxima corresponding to $t_{ia}/t_{ref} = 5.3$ ($A = 2$) and $t_{ia}/t_{ref} = 4.6$ ($A = 0.5$). Fig. 17 shows the same behavior as already observed for $A = 1$, see Section 5.1, i.e. the curves of the spin-up and the RMF pulse at each given A proceed in close analogy from the instant of switching off the RMF (first maxima in U_{rz} marked by circles) until the first minimum in U_{rz} (squares in Fig. 17). Figs. 18 and 19 depict the snapshots of the fluid flow corresponding to the first maxima and minima in U_{rz} for $A = 0.5$ and $A = 2$, respectively. Figs. 18(b), (c) and 19(b), (c) clearly prove the similarity of the flow pattern at the first U_{rz} minimum between spin-down after the RMF pulse and the spin-up also for aspect ratios different from unity. The analysis of Figs. 5(c), 18(c) and 19(c), which are snapshots of the fluid flow at the time of the first U_{rz} minima, shows similarities in meridional flow patterns for $A = 1$ and $A = 0.5$ but not with $A = 2$. This phenomenon is explained by the dependence of the pressure distribution on the aspect ratio of the cavity, see the work of Nikrityuk et al. [31].

References

[1] A.A. Tsavaras, H.D. Brody, Electromagnetic stirring and continuous casting-achievements, problems and goals, J. Metals 167 (1984) 31–37.

[2] P.A. Davidson, An Introduction to Magnetohydrodynamics, Cambridge University Press, 2001.
[3] H.P. Greenspan, The Theory of Rotating Fluids, Breukelen Press, Brookline, 1990.
[4] S. Eckert, B. Willers, P.A. Nikrityuk, K. Eckert, U. Michel, G. Zouhar, Application of a rotating magnetic field during directional solidification of Pb–Sn alloys: consequences on the CET, Mat. Sci. Eng. A 413–414 (2005) 211–216.
[5] P.A. Nikrityuk, K. Eckert, R. Grundmann, A numerical study of unidirectional solidification of a binary metal alloy under influence of a rotating magnetic field, Int. J. Heat Mass Transfer 49 (2006) 1501–1515.
[6] D.G. Neilson, F.P. Incropera, Effect of rotation on fluid motion and channel formation during unidirectional solidification of a binary alloy, Int. J. Heat Mass Transfer 36 (1993) 489–505.
[7] G.P. Neitzel, S.H. Davis, Centrifugal instabilities during spin-down to rest in finite cylinders. Numerical experiments, J. Fluid Mech. 102 (1981) 329–352.
[8] A. Yeckel, J.J. Derby, Effect of accelerated crucible rotation on melt composition in high-pressure vertical Bridgmann growth of cadmium zinc telluride, J. Crystal Growth 209 (2000) 734–750.
[9] C.W. Lan, Flow and segregation control by accelerated rotation for vertical Bridgman growth of cadmium zinc telluride: ACRT versus vibration, J. Crystal Growth 274 (2005) 379–386.
[10] W.C. Yu, Z.B. Chen, W.T. Hsu, B. Roux, T.P. Lyubimova, C.W. Lan, Reversing radial segregation and suppressing morphological instability during Bridgman crystal growth by angular vibration, J. Crystal Growth 271 (2004) 474–480.
[11] P.W. Duck, M.R. Foster, Spin-up of homogeneous and stratified fluids, Annu. Rev. Fluid Mech. 33 (2001) 231–263.
[12] D.T. Valentine, K.D. Miller, Generation of ring vortices in axisymmetric spin-down: A numerical investigation, Phys. Fluids 6 (1994) 1535–1547.
[13] J.M. Lopez, P.D. Weidman, Stability of stationary endwall boundary layers during spin-down, J. Fluid Mech. 326 (1996) 373–398.
[14] X. Cui, A numerical study of the recirculation zones during spin-up and spin-down for confined rotating flows, Theor. Comput. Fluid Dynamics 17 (2003) 31–49.
[15] S. Kojima, T. Ohnishi, T. Mori, K. Shiwaku, I. Wakasugi, M. Ohgami, Application of advanced melt stirring to a new bloom caster, in: Proceedings of 66th Steelmaking Conf., The Iron and Steel Society of AIME, Atlanta, GA, 1983, pp. 127–131.
[16] P.A. Davidson, The interaction between swirling and recirculating velocity components in unsteady, inviscid flow, J. Fluid Mech. 209 (1989) 35–55.
[17] P.A. Davidson, F. Boysan, Oscillatory recirculation induced by intermittent, rotary, magnetic stirring, Ironmaking and Steelmaking 18 (1991) 245–252.
[18] I. Grants, G. Gerbeth, Linear three-dimensional instability of a magnetically driven rotating flow, J. Fluid Mech. 463 (2002) 229–239.
[19] A. Randriamampianina, R. Schiestel, W. Wilson, The turbulent flow in an enclosed corotating disk pair: axisymmetric numerical simulation and Reynolds stress modelling, Int. J. Heat Fluid Flow 25 (2004) 897–914.
[20] P.A. Nikrityuk, K. Eckert, R. Grundmann, Numerical study of a turbulent swirling flow of a liquid metal driven by a Lorentz force, in: K. Hanjalic, Y. Nagano, S. Jakirlic (Eds.), Turbulence, Heat Mass, Transfer, vol. 5, Begell House, 2006, pp. 477–480.
[21] P.A. Nikrityuk, K. Eckert, R. Grundmann, Axisymmetric modelling of the mixing of two miscible liquid metals driven by a rotating magnetic field, in: CD Proceeding of the Conference on Turbulence and Interactions TI2006, Porquerolles, France, May 28–June 2, 2006.
[22] Ph. Marty, L. Martin Witkowski, P. Trombetta, T. Tomasino, J.P. Garandet, On the stability of rotating MHD flows, in: A. Alemany, P. Marty, J.P. Thibault (Eds.), Transfer Phenomena in Magnetohydrodynamics and Electroconducting Flows, Kluwer Academic Publisher, Dordrecht, 1999.
[23] Yu.M. Gelfgat, J. Priede, MHD flows in a rotating magnetic field (a review), Magnetohydrodynamics 31 (1995) 188–200.
[24] J. Priede, Yu.M. Gelfgat, Mathematical model of the mean electromagnetic forces induced by a rotating magnetic field in a liquid column of a finite length, Magnetohydrodynamics 32 (1996) 249–256.
[25] L.P. Gorbachev, V.N. Nikitin, A.L. Ustinov, Magnetohydrodynamic rotation of an electrically conductive liquid in a cylindrical vessel of finite dimensions, Magnetohydrodynamics 10 (1974) 406–414.
[26] L. Martin Witkowski, J.S. Walker, Ph. Marty, Nonaxisymmetric flow in a finite-length cylinder with a rotating magnetic field, Phys. Fluids 11 (1999) 1821–1826.
[27] P.A. Nikrityuk, K. Eckert, R. Grundmann, Rotating magnetic field-driven flows in conductive inhomogeneous media: Part I – Numerical study, Met. Mat. Trans. B 37 (2006) 349–359.
[28] P.A. Nikrityuk, K. Eckert, R. Grundmann, Numerical study of spin-up dynamics of a liquid metal stirred by rotating magnetic fields in a cylinder with the upper free surface, Magnetohydrodynamics J. 40 (2004) 127–146.
[29] M. Ungarish, The spin-up of liquid metal driven by a rotating magnetic field, J. Fluid Mech. 347 (1997) 105–118.
[30] P.A. Nikrityuk, M. Ungarish, K. Eckert, R. Grundmann, Spin-up of a liquid metal flow driven by a rotating magnetic field in a finite cylinder. A numerical and analytical study, Phys. Fluids 17 (2005) 067101–0671016.
[31] P.A. Nikrityuk, K. Eckert, R. Grundmann, Numerical study of a laminar melt flow driven by a rotating magnetic field in enclosed cylinders with different aspect ratios, Acta Mech. 186 (2006) 17–35.
[32] J.H. Ferziger, M. Peric, Computational Methods for Fluid Dynamics, second ed., Springer-Verlag, Berlin, 2002.
[33] C.M. Rhie, W.L. Chow, Numerical study of the turbulent flow past an airfoil with trailing edge separation, AIAA 21 (1983) 1525–1532.
[34] H.L. Stone, Iterative solution of implicit approximations of multidimensional partial differential equations, SIAM J. Numer. Anal. 5 (1968) 530–558.
[35] Y. Takeda, Development of an ultrasound velocity profile monitor, Nucl. Eng. Design 126 (1991) 277–284.
[36] D. Brito, H.-C. Nataf, P. Cardin, J. Aubert, J.P. Masson, Ultrasonic Doppler velocimetry in liquid gallium, Exp. Fluids 31 (2001) 653–663.
[37] S. Eckert, G. Gerbeth, Velocity measurements in liquid sodium by means of ultrasound Doppler velocimetry, Exp. Fluids 32 (2002) 542–546.
[38] A. Cramer, C. Zhang, S. Eckert, Local flow structures in liquid metals measured by ultrasonic Doppler velocimetry, Flow Meas. Instrum. 15 (2004) 145–153.

[39] J. Stiller, K. Frana, A. Cramer, Transitional and weakly turbulent flow in a rotating magnetic field, Phys. Fluids 18 (2006) 074105.
[40] K. Frana, J. Stiller, R. Grundmann, Transitional and turbulent flows driven by a rotating magnetic field, Magnetohydrodynamics 42 (2006) 187–197.
[41] P.A. Nikrityuk, K. Eckert, R. Grundmann, Verfahren zum Rühren von leitenden Flüssigkeiten in Behältern, German Patent DE 102004017443.